Compound wind and rainfall extremes: Drivers and future changes over the UK and Ireland

Colin Manning [a,*], Elizabeth J. Kendon [b], Hayley J. Fowler [a,c], Jennifer L. Catto [d], Steven C. Chan [e], Philip G. Sansom [f]

[a] School of Civil Engineering and Geosciences, Newcastle University, Newcastle upon Tyne, United Kingdom
[b] Met Office Hadley Centre, Exeter, United Kingdom
[c] Tyndall Centre for Climate Change Research, Newcastle University, United Kingdom
[d] Department of Mathematics and Statistics, University of Exeter, Exeter, EX4 4QE, United Kingdom
[e] National Oceanography Centre, Southampton, SO14 3ZH, United Kingdom
[f] Met Office, FitzRoy Road, Exeter, EX1 3PB, United Kingdom

ABSTRACT

The co-occurrence of wind and rainfall extremes can yield larger impacts than when either hazard occurs in isolation. This study assesses compound extremes produced by Extra-tropical cyclones (ETCs) during winter from two perspectives. Firstly, we assess ETCs with extreme footprints of wind and rainfall; footprint severity is measured using the wind severity index (WSI) and rain severity index (RSI) which account for the intensity, duration, and area of either hazard. Secondly, we assess local co-occurrences of 6-hourly wind and rainfall extremes within ETCs. We quantify the likelihood of compound extremes in these two perspectives and characterise a number of their drivers (jet stream, cyclone tracks, and fronts) in control (1981–2000) and future (2060–2081, RCP8.5) climate simulations from a 12-member ensemble of local convection-permitting 2.2 km climate projections over the UK and Ireland. Simulations indicate an increased probability of ETCs producing extremely severe WSI and RSI in the same storm in the future, occurring 3.6 times more frequently (every 5 years compared to every 18 years in the control). This frequency increase is mainly driven by increased rainfall intensities, pointing to a predominantly thermodynamic driver. However, future winds also increase alongside a strengthened jet stream, while a southward displaced jet and cyclone track in these events leads to a dynamically-enhanced increase in temperature. This intensifies rainfall in line with Clausius-Clapeyron, and potentially wind speeds due to additional latent heat energy. Future simulations also indicate an increase in the land area experiencing locally co-occurring wind and rainfall extremes; largely explained by increased rainfall within warm and cold fronts, although the relative increase is highest near cold fronts suggesting increased convective activity. These locally co-occurring extremes are more likely in storms with severe WSI and RSI, but not exclusively so as local co-occurrence requires the coincidence of separate drivers within ETCs. Overall, our results reveal many contributing factors to compound wind and rainfall extremes and their future changes. Further work is needed to understand the uncertainty in the future response by sampling additional climate models.

1. Introduction

The co-occurrence of wind and rainfall extremes may yield larger impacts than when either hazard occurs in isolation. This interaction, termed a compound event (Zscheischler et al., 2018), can occur across varying time and spatial scales (Tilloy et al., 2022; Bloomfield et al., 2023) such as temporal clustering of windstorms in a single season bringing widespread impacts combined with regional flooding (Kendon and McCarthy, 2015), leading to large aggregate losses as seen for the rail sector in the UK (Hillier et al., 2015, 2020). In a single storm, coastal flooding can be enhanced through the combination of heavy rainfall over a river basin and a wind-driven storm surge (Bevacqua et al., 2017; Ward et al., 2018; Couasnon et al., 2020), emergency service resources may be stretched by the simultaneous occurrence of extremes in separate locations, while horizontally-blown rainfall in the presence of strong winds elevates the risk of moisture related deterioration in

buildings (Zhou et al., 2016; Kubilay et al., 2021; Støver et al., 2022; Gholamalipour et al., 2022). Tilloy et al. (2022) nicely illustrate the spatiotemporal compounding nature of wind and rainfall hazards over the UK in terms of their footprints, the area affected by individual extremes, and the degree to which their footprints may overlap.

A large body of literature has already demonstrated a robust statistical link between wind and rainfall over different spatiotemporal scales (Raveh-Rubin and Wernli, 2015; Hillier and Dixon, 2020; Hénin et al., 2021; De Luca et al., 2020; Tilloy et al., 2022). For instance, studies have assessed the probability of wind and rain jointly exceeding high thresholds, such as their 98th percentiles, at the same time and location, or within a certain distance and/or time frame of one another (Martius et al., 2016; Bevacqua et al., 2019; Ridder et al., 2020; Owen et al., 2021a, 2021b; Vignotto et al., 2021; Zscheischler et al., 2021). Spatial and temporal criteria are imposed with the knowledge that wind and rainfall extremes occur due to different processes at different locations and times within the same storm system.

Underpinning these extremes is the day-to-day variability of weather systems. In particular, extra-tropical cyclones (ETCs) provide an environment comprised of multiple coherent air streams and fronts that produce wind and rainfall extremes both together and in isolation (Pfahl and Wernli, 2012; Pfahl, 2014; Hénin et al., 2021; Catto and Dowdy, 2021; Owen et al., 2021b; Messmer and Simmonds, 2021). A warmer climate is likely to bring more intense ETCs (Catto et al., 2019) with higher rainfall (Berthou et al., 2022), stronger winds (Zappa et al., 2013; Priestley and Catto, 2022a; Manning et al., 2023; Little et al., 2023) and an increased frequency of co-located wind and rainfall extremes (Bevacqua et al., 2019, 2020a; Ridder et al., 2022; François and Vrac, 2023). However, we do not have an in depth understanding around the drivers of co-occurring extremes, for example what factors cause co-occurring extremes and their future increases.

Within ETCs, rainfall extremes often precede wind extremes (Bengtsson et al., 2009). Rainfall extremes occur largely in the warm sector due to the uplift of air over warm and cold fronts (Catto and Pfahl, 2013; Utsumi et al., 2017), the ascent of the warm conveyor belt (WCB) over these fronts (Pfahl et al., 2014; Catto et al., 2015), and convection embedded within the WCB close to the cold front (Oertel et al., 2021). Further factors influence rainfall intensity; these include the strength of frontal gradients (Catto and Pfahl, 2013), which are stronger in the presence of dry intrusions (Raveh-Rubin and Catto, 2019), as well as the temperature and moisture availability within an ETC (Berthou et al., 2022). The strongest winds occur in the cold sector of ETCs, following the passage of the cold front, driven by tight pressure gradients and coherent air streams on the equatorward side of a cyclone's centre, namely the sting jet and the cold conveyor belt (CCB) (Hewson and Neu, 2015; Hart et al., 2017; Manning et al., 2022). Strong winds can also arise due to the WCB in the warm sector, the rearward moving component of the CCB on the poleward side of ETCs (Gentile and Gray, 2023), as well as from convectively-driven gusts near to the cold front (Earl et al., 2017; Earl and Simmonds, 2019; Eisenstein et al., 2022). Wind and rainfall extremes can co-occur at the same time and location because of shared drivers within ETCs, such as the WCB and convective processes near to the cold front (Ludwig et al., 2015; Raveh-Rubin and Wernli 2016). Furthermore, co-occurrences may also arise from coincident separate drivers such as frontal rainfall over areas of tight pressure gradients.

Not all the above contributors will be present in each ETC, nor will they always produce extremes: the likelihood of extremes is also dependent on the large-scale dynamical environment surrounding ETCs. For instance, ETCs producing extreme rainfall alone are often slower moving (Owen et al., 2021b) and have different jet stream characteristics (Raveh-Rubin and Wernli, 2015) than those that produce extreme winds alone. ETC speed may influence the duration of rainfall, while a strong jet stream may intensify windstorms leading to stronger wind speeds. Jet stream orientation will also determine the path of an ETC, its impact location and whether an ETC comes from more southerly latitudes, bringing warm, moist air that contributes to rainfall extremes.

In this article, we assess compound wind and rainfall extremes within ETCs in control (1980–2000) and future climate (2060–2080, RCP8.5) simulations produced by a 12-member ensemble of very high-resolution (2.2 km) convection-permitting climate simulations over the UK and Ireland (the "UKCP Local" projections, Kendon et al., 2021a). We approach compound extremes from two perspectives. 1) we assess ETCs with co-occurring extreme footprints of wind and rainfall which accounts for large areas of wind and rainfall extremes occurring in the same ETC, but not necessarily in the same location; 2) we assess local co-occurrences of 6-hourly wind and rainfall extremes (99th percentile) within ETCs. In both perspectives, we aim to assess projected future changes in compound wind-rainfall extremes and understand contributions of drivers such as the jet stream, cyclone track, and fronts.

2. Data

We use a 12-member ensemble of very high-resolution (2.2 km) convection-permitting climate model (CPM) over the UK and Ireland (Kendon et al., 2021a) for a control (December 1980–November 2000) and a future (December 2060–November 2080, RCP8.5 scenario) simulation. The boundaries of the CPM domain are provided in Fig. 3a, though the outer 95 grid cells (209 km) are excluded to avoid boundary effects. These simulations were produced as part of the UK Climate Projections (UKCP) by the UK Met Office (Lowe et al., 2018; Murphy et al., 2018) and include global climate model (GCM) projections (~60 km), regional climate model (RCM) projections over Europe (~12 km) and the set of local CPM projections over the UK and Ireland. The projections are produced by perturbing uncertain parameters in the GCM (Murphy et al., 2018), providing boundary conditions for the RCM. Uncertain parameters in the RCM are also perturbed in the same way as the GCM and this provides boundary conditions for the CPM. No perturbations are applied to the CPM as there is no way to perturb the CPM that is consistent with the coarse models due to differences in physics, and so the CPM ensemble samples uncertainty in the large-scale driving conditions and natural variability. The small CPM domain means that it is reasonably constrained by the large-scale conditions provided by the RCM at its boundary, which in turn is conditioned by the large-scale information provided by the GCM such as cyclones, fronts as well as upper-level winds and temperature gradients.

We assess wind gusts and rainfall from the CPM only over the UK and Ireland land areas. The CPM is chosen over its coarser resolution counterparts for wind gusts and rainfall due to its explicit representation of convection that leads to better representation of extreme rainfall (Chan et al., 2014; Kendon et al., 2021b, 2023) and wind speeds (Manning et al., 2022, 2023). We combine the information from the CPM with large-scale information from the GCM for the analysis of drivers such as cyclones and the jet stream, as well as data from the RCMs for the identification of frontal features as described below. Although the CPM is largely constrained by these models, we do make some allowances for potential difference between the simulations as detailed in the methods.

3. Methods

3.1. Cyclone and front identification

We use an event-based analysis based on the occurrence of an extra-tropical cyclone (ETC) over the UK and Ireland within the CPM domain. Only ETCs occurring in the winter season (DJF) are considered. ETC positions are identified at 6-hourly intervals (00, 06, 12, 18 h) for all years analysed in the GCM (Control: 1981–2000; Future: 2061–2080) using the Hoskins and Hodges (2002) tracking algorithm, which identifies and tracks ETCs based on 850 hPa relative vorticity regridded to a T42 grid (~300 km) resolution. These positions are also used to indicate the location of ETCs for the CPM domain as we do not find large

differences in positions of ETCs between the CPM and its parent GCM, in a visual assessment of the 200 most severe windstorms (Manning et al., 2023). To link wind and rainfall extremes to ETCs, we only consider grid cells within 1000 km of the centre of the ETC which allows for any slight discrepancies in the position of ETCs in the CPM and GCM. This is a commonly used threshold and we do not expect results to be sensitive to this choice, as demonstrated in Bevacqua et al. (2020b).

We assess the contribution of three frontal areas within this analysis. These include a cold frontal area, a warm frontal area, and an overlap area where identified cold and warm fronts occur in proximity. Fronts are identified using an algorithm described in Sansom and Catto (2022) which is based on the previous algorithms of Hewson (1998) and Berry et al. (2011). The algorithm firstly identifies frontal line features using wet bulb potential temperature (ϑ_W) at 850 hPa at the same 6-hourly intervals as the ETCs, and then classifies frontal points into warm and cold fronts using u and v wind components at 850 hPa. See Sansom and Catto (2022) for more detail and examples. To link wind and rainfall extremes with fronts, the frontal line features are expanded by 250 km around each grid cell through which a frontal line passes to produce a frontal area. Often the identified cold and warm fronts occur in proximity causing their expanded frontal areas to overlap. We therefore define a third category called a frontal overlap area as it is difficult to determine which front (cold or warm) a hazard is associated with. All grid cells that fall within the warm, cold and frontal overlap areas, exclusively, are included in the calculation of metrics for those frontal areas. Only fronts occurring within 1000 km of the centre of an ETC are considered here. Fronts are identified in the RCM simulation, that provides the boundary conditions for the CPM, and are used to provide the location of fronts within the CPM simulation. As the large-scale variability of the CPM is constrained by the RCM, we do not expect large deviations in the position of fronts between the two models, though this has not been explicitly tested.

3.1.1. Cyclone composites

Cyclone composites are produced using a technique employed by many previous studies (e.g. Bengtsson et al., 2007; Catto et al., 2010; Dacre et al., 2012; Sinclair et al., 2020; Priestley and Catto, 2022a). The composites are used to demonstrate where wind, rainfall and co-located extremes occur within an ETC relative to its centre. ETCs are centred with respect to the position of the minimum sea level pressure (MSLP) in the RCM within a 500 km radius of the ETC centre provided by the tracking algorithm. The use of the ETC centre from the RCM fine tunes the centre of the ETC to be as close as possible to that of the CPM when producing composites, it also avoids issues that occur when the cyclone is positioned close to the CPM boundary, if one used MSLP from the CPM. To account for differences in the direction of ETCs, all fields are rotated and aligned so that ETCs are travelling eastwards.

3.2. Wind and rainfall footprint severity metrics

For each cyclone and frontal area, we quantify the severity of its wind and rainfall footprints using a wind severity index (WSI) based on 6-hourly maximum wind gusts and a rainfall severity index (RSI) based on 6-hourly accumulated rainfall. The 6-hourly periods are centred around the 6-hourly intervals used by the cyclone and front algorithms (i.e., 03h–09h is used for 06h). These indices follow a similar approach to the Storm Severity Index (SSI) (Leckebusch et al., 2008) that links the cube of surface winds exceeding an extreme threshold to insured losses (e.g. Osinski et al., 2016). Note, we do not cube the wind or rainfall exceedance here as there is no known premise to do so for rainfall. The WSI is calculated using 6-hourly wind gusts as:

$$WSI_{T,K} = \sum_{t=1}^{T} \sum_{k=1}^{K} \left[\max\left(1, \frac{v_{k,t}}{v_{99,k}}\right) - 1 \right], \qquad (1)$$

where $v_{k,t}$ represents the wind gust at time t and grid cell k, and $v_{99,k}$ is

the 99th percentile of 6-hourly winds at grid cell k estimated from the winter months in the control simulation. Similarly, the RSI is calculated using 6-hourly accumulated rainfall as:

$$RSI_{T,K} = \sum_{t=1}^{T} \sum_{k=1}^{K} \left[\max\left(1, \frac{r_{k,t}}{r_{99,k}}\right) - 1 \right], \qquad (2)$$

where $r_{k,t}$ represents the accumulated rainfall at time t and grid cell k, and $r_{99,k}$ is the 99th percentile of 6-hourly accumulated rainfall at grid cell k estimated from the winter months in the control simulation. In other words, the WSI and RSI are the sum of all scaled exceedances of the local 99th percentiles in an ETC, thereby accounting for the overall intensity, duration, and area of extremes in an ETC.

3.2.1. Estimation of univariate and bivariate return periods

Return periods (RPs) are estimated for events from the pooled 12-member ensemble that provides 240 years of simulated data (12 members x 20 years) for both the control and future periods. Only winter months (December, January and February) are considered. Univariate RPs are estimated for WSI and RSI return levels separately in a stationary framework, in which all events are treated as independent. We use a peak over threshold (PoT) approach and fit a Generalised Pareto Distribution (GPD) to the top 5% of WSI and RSI events (WSI^{uni} and RSI^{uni}) for control and future periods separately.

We also quantify bivariate RPs, which represent the expected waiting time between events in which specified values of WSI and RSI are jointly exceeded. Following an approach applied in previous studies (Bevacqua et al., 2019; Manning et al., 2019), bivariate RPs are estimated through a PoT approach in which a parametric copula-based probability distribution is applied to events in which both WSI and RSI exceed their respective 95th percentiles. The 95th percentiles are defined from the control simulation and are demonstrated by the solid horizontal and vertical black lines in Fig. 1a and b. The bivariate RP for jointly exceeding the τ-year univariate return levels WSI_τ and RSI_τ is then estimated as:

$$T(WSI_\tau, RSI_\tau) = \frac{\mu_E}{1 - u_{WSI_\tau} - u_{RSI_\tau} + C(u_{WSI_\tau}, u_{RSI_\tau})}, \qquad (3)$$

where $\mu_E = N_Y/N_E$ is the average inter-arrival time of events where WSI and RSI jointly exceed their 95th percentiles, u_{WSI_τ} and u_{RSI_τ} are the univariate cumulative probabilities of a given τ-year univariate return level, while C represents the copula which models the bivariate distribution of WSI and RSI. For details on copula and the procedure followed in fitting the statistical model, see Appendix B. We estimate bivariate RPs in control and future climates to quantify the change in RPs. We also estimate the contribution of changes in WSI, RSI and the (WSI, RSI) dependence to the projected change in bivariate RPs. This methodology is also outlined in Appendix B.

Uncertainties in the univariate and bivariate RPs are estimated by applying non-parametric bootstrapping in which we sample 1000 times, with replacement, individual winters to preserve the serial dependence within seasons and to account for interannual variability between seasons. For each sample bootstrap, we calculate the RPs, giving 1 000 estimated RPs. The expected RP is then calculated as the median of this sample, while the 95% uncertainty interval is the range between the 2.5th and 97.5th percentiles.

3.2.2. Categorising events according to RSI and WSI

Within the analysis, we identify why an ETC might produce an extreme wind footprint or rainfall footprint only, and why one may produce both extremes in the same event. To do so, we combine events into three categories based on their 1-year return levels from the control (*cntl*; $RL1_{RSI}^{cntl}$; $RL1_{WSI}^{cntl}$) and future (*fut*; $RL1_{RSI}^{fut}$; $RL1_{WSI}^{fut}$) simulations. In a given simulation (*sim*: *cntl* or *fut*), an event e_i^{sim} with rsi_i^{sim} and wsi_i^{sim} is assigned to one of three categories: E_{RSI}^{sim} (events where only RSI exceeds

its 1-yr return level); E_{WSI}^{sim} (events where only WSI exceeds its 1-year return level); and E_{Comp}^{sim} (events where both RSI and WSI exceed their respective 1-year return levels). These criteria are summarised in Table 1 along with the number of events within each category.

The use of the 1-year return level defined from each simulation respectively ensures a similar number of events are used in producing the composites, which allows us to assess the average characteristics and possible reasons for differences between extreme events of similar frequencies in the control and future simulations. It should be noted that the frequency of events in E_{Comp}^{sim} can change if the correlation changes between *RSI* and *WSI* such that they become more/less dependent. However, we do not observe a change in correlation, and event numbers in each category are similar in control and future simulations.

3.3. Local co-occurrences of extreme wind gusts and rainfall

We identify cases where the 6-hourly maximum wind gust and 6-hourly rainfall accumulation exceed their respective 99th percentiles at the same time and grid cell in control and future simulations. The 99th percentiles are defined from the control simulations. For each ETC, we then quantify the metric A_{Comp}, the percentage of land area that experiences a co-occurrence at least once during an event. Hence, if a grid cell experiences more than one co-occurrence in an event, it will only be counted once.

We also assess the contribution from wind and rainfall intensity changes to the changes in A_{Comp} within the future simulations. The wind intensity-driven change to A_{Comp} is identified by removing the rainfall intensity-driven change. To do so, we recalculate A_{Comp} for co-occurrences in future simulations when wind gusts exceed their 99th percentiles, defined from the control simulations, at the same time as rainfall exceeds its 99th percentile defined from the future simulations. The latter removes changes in A_{Comp} that occur due to a simple shift in the rainfall distribution while conserving the change in A_{Comp} due to a shift in the wind gust distribution. This provides a first approximation of wind intensity-driven changes in A_{Comp}. The procedure is then reversed to assess the rainfall intensity-driven changes in A_{Comp}.

4. Results

The results section is structured in two main parts. Firstly, we present results related to the wind and rainfall severity indices, WSI and RSI. And secondly, we present results on the area of locally co-occurring 6-hourly wind-rainfall extremes within ETCs (A_{Comp}). In both parts, we assess future changes in these metrics and characterise drivers of these compound hazards in control and future simulations. The assessed drivers of WSI and RSI include the jet stream and cyclone tracks, while the assessed drivers of A_{Comp} include features within ETCs such as warm and cold fronts.

4.1. Assessment of wind and rainfall footprint severity (WSI and RSI)

The severity of wind and rainfall footprints over land grid cells are

Table 1
Description of criteria used for the three event categories E_{WSI}^{sim}, E_{RSI}^{sim}, and E_{Comp}^{sim} as well as the number of events per category (N) in control and future simulations.

Event Type	Criteria	Description	N (Control, Future)
E_{WSI}^{sim}	$wsi_i^{sim} > RL1_{WSI}^{sim}$, $rsi_i^{sim} < RL1_{RSI}^{sim}$	Only WSI exceeds 1-year RL	199, 205
E_{RSI}^{sim}	$rsi_i^{sim} > RL1_{RSI}^{sim}$, $wsi_i^{sim} < RL1_{WSI}^{sim}$	Only RSI exceeds 1-year RL	199, 192
E_{Comp}^{sim}	$wsi_i^{sim} > RL1_{WSI}^{sim}$, $rsi_i^{sim} > RL1_{RSI}^{sim}$	Both WSI and RSI exceed 1-year RLs	41, 40

quantified using the WSI (Eq. (1)) and RSI (Eq. (2)) respectively. We first explore the relationship between WSI and RSI and quantify the likelihood joint extremes in ETCs within control and future simulations. Fig. 1a and b demonstrates the (WSI, RSI) dependence within individual ETCs (grey dots). In both control and future simulations, the most extreme WSI and RSI tend to occur in isolation, while joint extremes are less frequent. For example, considering WSI alone, an event with WSI exceeding 250 (vertical blue line in Fig. 1a) has a univariate RP of 2 years in the control simulation. The equivalent RSI value with a RP of 2 years is 300 (horizontal blue line). For both WSI and RSI to jointly exceed these 2-year return levels (blue dot), the bivariate RP (black contours) is approximately 18 years. However, this frequency increases in the future simulations.

The estimated univariate and bivariate return periods (RPs) are presented in Fig. 1c–e. A statistically significant future increase in WSI and RSI return levels (RLs) is seen at all RPs from 1 to 20 years; expected RLs in the future period are outside the respective 95% uncertainty intervals estimated from the control period. Future increases are much larger for the RSI (~90% higher) than the WSI RLs (~25% higher). We also find a statistically significant increase in the joint probability (i.e. decrease in bivariate RP) of WSI and RSI exceeding the 1–10 year univariate RL thresholds defined from the control simulation (Fig. 1e). For example, the bivariate RP for a joint exceedance of their respective 2-year RLs from the control simulation (blue dot in Fig. 1a and b) decreases from 18 years to 5 years, meaning that such events are ~3.6 times more frequent in future simulations. Furthermore, the contours in Fig. 1a and b that present the bivariate RPs for jointly exceeding WSI and RSI values on the corresponding x- and y-axes are lower across the 2D matrix in the future (Fig. 1b), meaning that the probability of jointly exceeding any WSI and RSI thresholds is increased in the future. This demonstrates that ETCs are generally windier and wetter in the future simulations.

Fig. 1e also presents the contributions to the increase in bivariate RPs due to changes in WSI, RSI and the (WSI, RSI) dependence. Changes in RSI are the primary driver of changes to bivariate RPs for joint exceedances of their respective 1–10 year RLs, as shown from comparison of the black lines in Fig. 1c. In contrast, changes in WSI provide a relatively small contribution above these thresholds. Lastly, there is no change in the dependence between WSI and RSI.

4.1.1. Influence of jet stream and cyclone tracks

The occurrence of extreme WSI and RSI in ETCs is largely constrained by drivers such as the jet stream and the track an ETC follows. For this reason, we assess characteristics of these drivers within three ETC categories E_{WSI}^{sim}, E_{RSI}^{sim} and E_{Comp}^{sim} in order to explain why some ETCs produce extremes of only WSI (E_{WSI}^{sim}) or RSI (E_{RSI}^{sim}), and why others produce both extremes (E_{Comp}^{sim}).

Fig. 2a and b presents the typical jet stream winds at 300 hPa for varying values of WSI and RSI in control and future simulations. E_{WSI}^{sim} ETCs tend to occur with a strong jet stream, while E_{RSI}^{sim} are characterised by a weaker jet stream, as illustrated by the gradient of low to high jet stream winds from left to right. This result is expected given a strong jet intensifies cyclones leading to higher winds, while a weaker jet causes cyclones to move more slowly allowing rainfall to persist for longer. This result is further demonstrated in Fig. 2d–f which presents the zonal mean wind speeds throughout the troposphere (black contours) during ETC events over the North Atlantic. These winds are stronger during E_{WSI}^{sim} (d, e) than E_{RSI}^{sim} ETCs (g, h), though E_{Comp}^{sim} cyclones show similar jet stream characteristics to the E_{WSI}^{sim} cyclones, indicating that a strong jet stream is a necessary condition for extreme WSI but not an inhibiting factor for extreme RSI.

There are also noteworthy differences in the ETC tracks of E_{WSI}^{sim} and E_{RSI}^{sim}. Fig. 3 provides tracks for all ETCs as well as for cyclones in each event category. E_{WSI}^{sim} tracks are more zonally elongated (Fig. 3d and e)
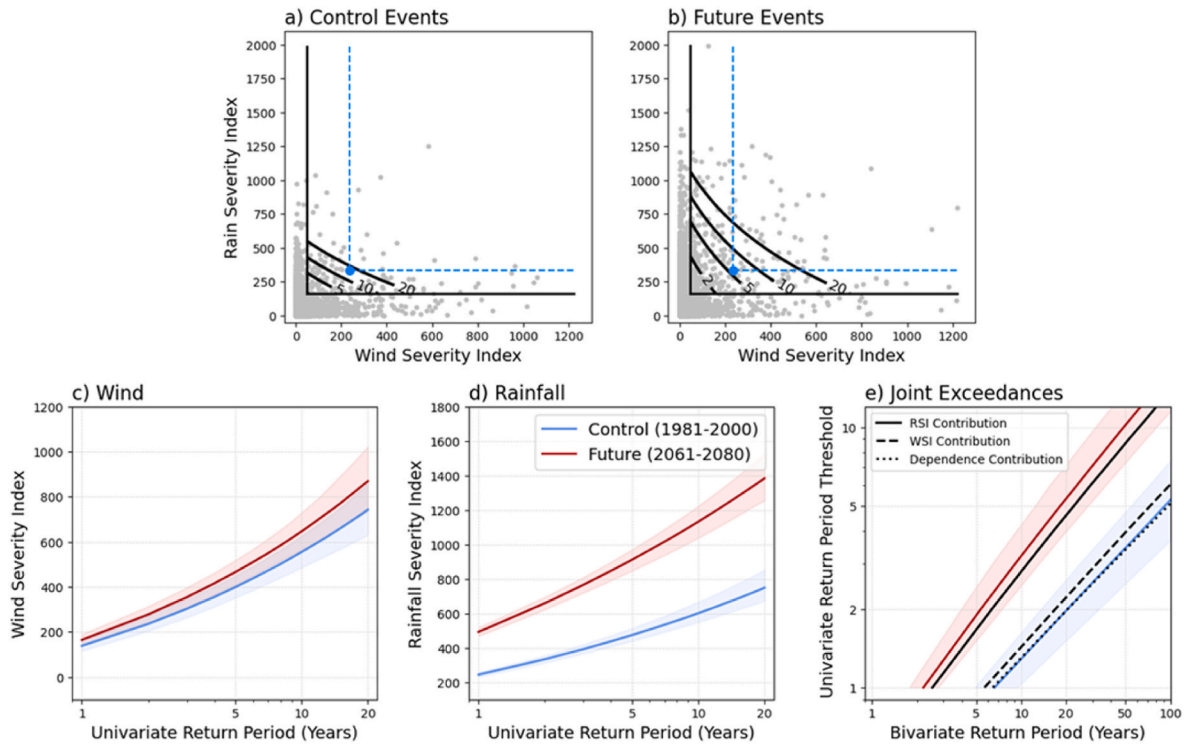
Fig. 1. Univariate and bivariate return periods (RPs) of WSI and RSI. Scatter plots illustrate WSI and RSI from events (grey dots) in the control (a) and future simulations (b). Black contours represent the quantified bivariate RPs obtained from the copula-based model fitted to RSI and WSI that jointly exceed their respective 95th percentiles from the control period (black horizonal and vertical lines). For demonstration purposes, a blue dot and lines are plotted at the univariate 2-year return levels of the WSI and RSI. Bottom row presents WSI (c) and RSI (d) return levels for RPs between 1 and 20 years in the control (blue line) and future (red line) simulations, as well as bivariate RPs (e) for joint exceedances of WSI and RSI above 1-10-year univariate return levels. Also shown are the future change in bivariate RPs (black lines) when accounting for changes in RSI only (solid line), WSI only (dashed line) and the dependence between WSI and RSI only (dotted line). (For interpretation of the references to colour in this figure legend, the reader is referred to the Web version of this article.)

than tracks for E_{RSI}^{sim} events (Fig. 3g and h) while the latter tend to reach lower latitudes close to the CPM domain, likely bringing warmer and moister air than E_{WSI}^{sim} ETCs. Furthermore, we see differences in the placement of tracks over the UK. E_{WSI}^{sim} cyclones are more likely to track over northern parts of the UK (Fig. 3d and e), while E_{RSI}^{sim} cyclones are more likely to track over the southern part of the UK (Fig. 3g and h). A direct comparison between the two cyclone types is given by the yellow and blue contours in the respective panels.

This spatial difference in ETC track frequencies near to the UK can be explained using the composites presented in Fig. 4: these show where the highest winds and rainfall tend to occur in an ETC relative to its centre. The strongest winds generally occur on the southern side of the ETC (Fig. 4a and b) while the highest rainfall occurs northeast of the ETC centre (Fig. 4d and e). Therefore, E_{WSI}^{sim} cyclones that track over the north of the domain produce high WSI and low RSI as the track maximises the area of land overlapping with the strongest winds in an ETC, while minimising the area of land that overlaps with the highest ETC rainfall. The opposite is the case for E_{RSI}^{sim} cyclones tracking over the south of the domain which produce low WSI and high RSI. Due to these characteristics, E_{Comp}^{sim} cyclones that produce both high WSI and high RSI over the UK and Ireland then tend to track through the centre of the domain (Fig. 3j and k) increasing the likelihood for large areas of land to experience both wind and rainfall extremes.

From the results, we infer that the placement of an ETC track has a large influence on extreme footprints over land in the domain, but they do not suggest fundamental differences in tracks associated with ETCs that produce extreme winds or rainfall at some point in their life cycle. We also note that these characteristics are different to those shown for all cyclones in Fig. 3a and b, highlighting that the track characteristics of regional extremes cannot be inferred from a general assessment of ETC

track frequency.

4.1.2. Projected changes in jet stream and cyclone tracks

The projected change in zonal winds and cyclone tracks are presented in Figs. 2 and 3, respectively, for all ETCs and for the three event categories E_{WSI}^{sim}, E_{RSI}^{sim} and E_{Comp}^{sim}. A general strengthening of zonal winds during all ETCs is seen throughout the troposphere (Fig. 2c), as well as across the Atlantic and over Europe at 300 hPa (see Figure A1 in Appendix A). This is accompanied by an eastward extension of the ETC tracks over northern parts of Europe in future simulations (Fig. 3c). Such changes in mean circulation will potentially influence the likelihood of extremes, although our results demonstrate that changes in jet stream and ETC track characteristics conditioned on extremes can differ and contrast to changes in mean circulation, as outlined below.

Changes in zonal mean wind speeds are stronger for E_{WSI}^{sim} cyclones (Fig. 2d) than for all cyclones (Fig. 2c), and the largest increases for E_{WSI}^{sim} cyclones are shifted further south of the core of the highest winds in the control, whereas no shift is seen for the all cyclones. Furthermore, a different response is found for E_{WSI}^{sim} cyclone tracks compared to all cyclones. For instance, there is a 10–15% increase in ETC track frequency for E_{WSI}^{sim} cyclones further west in the future than in the control (Fig. 3f), while 10–15% of E_{WSI}^{sim} cyclones in the future simulations are shifted northward over the UK with a corresponding decrease in cyclones that propagate into northern parts of Europe such as Denmark and Germany. This is in direct contrast to the increase in overall cyclone frequency in this region (Fig. 3c) and would potentially lead to a reduced spatial dependence in wind damages from individual storms between those areas and the UK (e.g. Dawkins and Stephenson, 2018).

Changes in jet stream winds and ETC tracks for E_{RSI}^{sim} cyclones are closer to that for all cyclones although differences exist. Similar in-
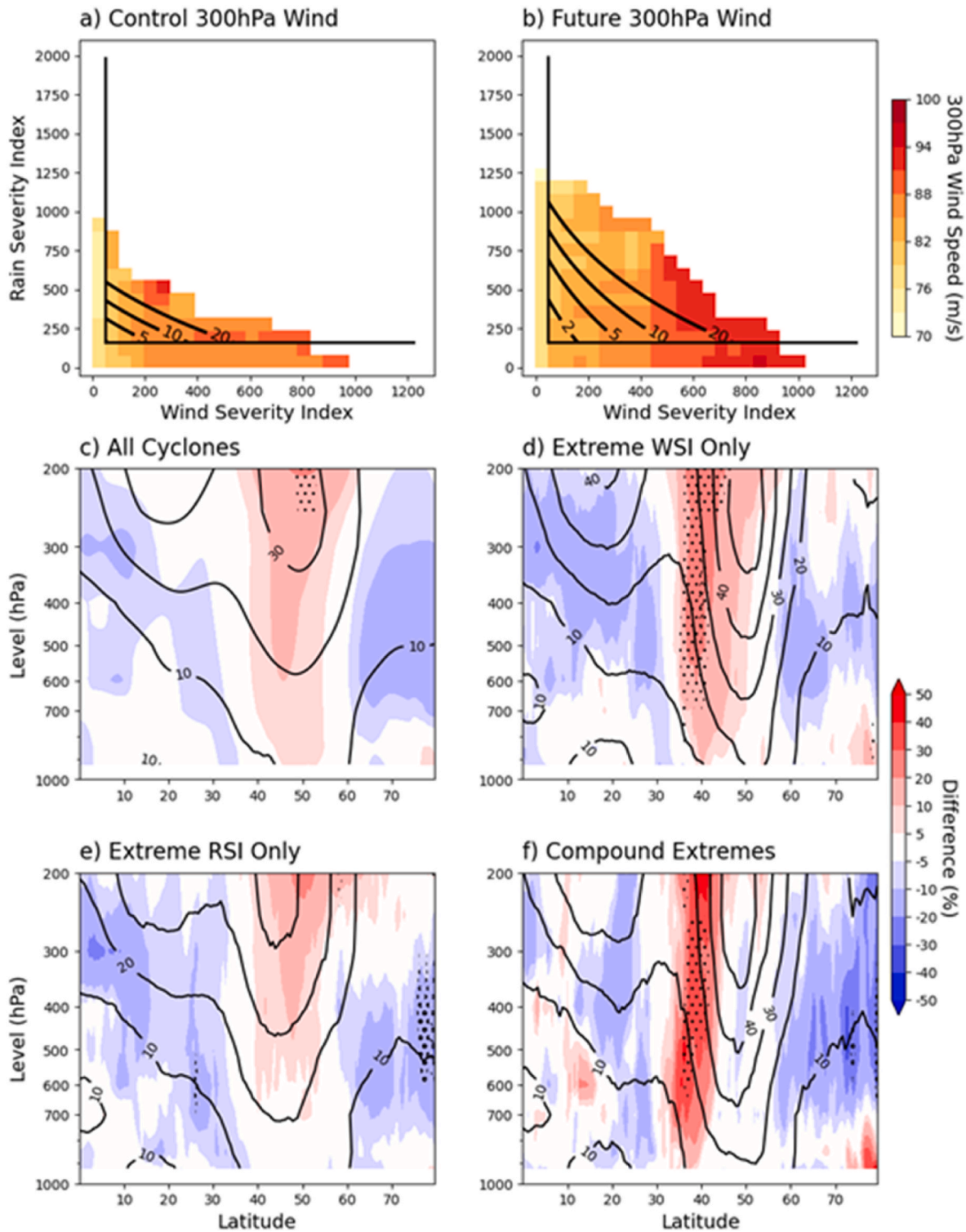
Fig. 2. Influence of the jet stream. Top row panels illustrate the maximum wind speed at 300 hPa from the GCM within 1 000 km the ETC centre in the control (a) and future (b) simulations. The shading represents the average of the maximum 300 hPa winds calculated from events that jointly exceed WSI and RSI thresholds (minimum of five events required). Middle and bottom rows present zonal mean wind speeds between 60°E and 30°W from control simulations (contours) and their future change (shading) for the different cyclone categories: (c) all cyclones; (d) E_{WSI}^{sim} (Extreme WSI only); (e) E_{RSI}^{sim} (Extreme RSI only); (f) and E_{Comp}^{sim} (compound extremes). Filled (unfilled) stippling for future changes indicates where at least 7 of 12 ensemble members agree on a positive (negative) change of 20%. Forward (backward) hatching indicate agreement in at least 9 of 12 members.

creases in zonal winds are found for E_{RSI}^{sim} cyclones though they are slightly weaker and the highest increases are found poleward of the highest zonal winds in the control (Fig. 2e). Changes to E_{RSI}^{sim} cyclone tracks also have a similar spatial signature to changes to all cyclones in

that more tracks extend over northern parts of Europe (Fig. 3i), although subtle differences are seen for changes in E_{RSI}^{sim} cyclone tracks where, in future simulations, 5–10% more ETCs come from a more southerly location; this is accompanied by a 5–10% reduction in ETCs further
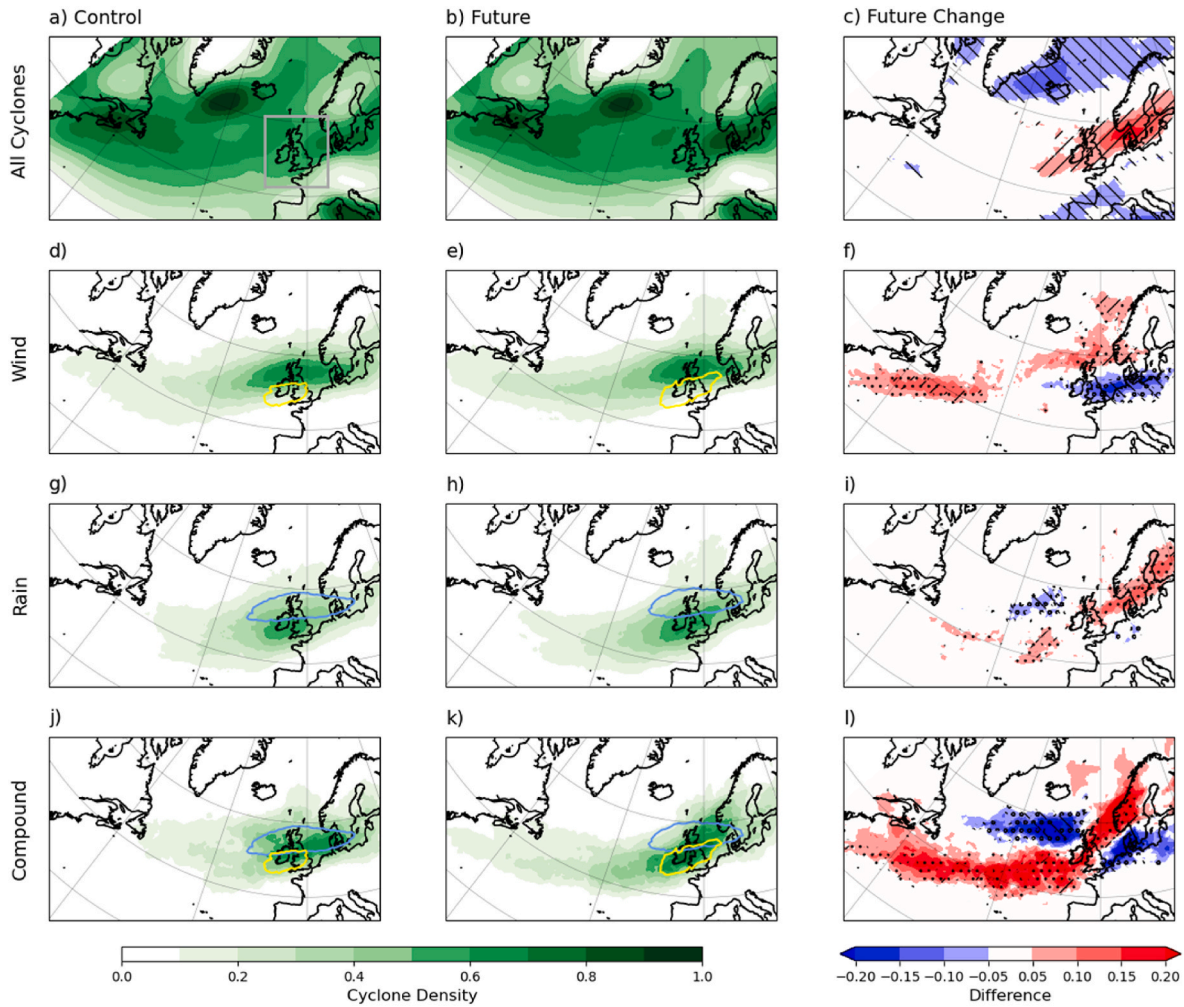
Fig. 3. Cyclone track densities from the Control (left column), Future (middle column) and future change (Future – Control). Track densities and their future change are given for all cyclones (top row – a-c) as well as cyclones in the three event types E_{WSI}^{sim} (Extreme WSI only – d-f), E_{RSI}^{sim} (Extreme RSI only – g-i), and E_{Comp}^{sim} (compound extremes – j-l). Densities in (a, b) are scaled with respect to the maximum density in (a) while densities in the three event categories are given as the proportion of the number of cyclones per category and simulation. Yellow contour lines represent the 50% frequency contour for E_{RSI}^{sim} cyclones in (d) and (e), while blue contour lines represent 50% frequency contour for E_{WSI}^{sim} cyclones in (g) and (h). Filled (unfilled) stippling for future changes (c, f, i, l) indicates where at least 7 of 12 ensemble members agree on a positive (negative) change of 0.05. Forward (backward) hatching indicate agreement in 9 of 12 members. (For interpretation of the references to colour in this figure legend, the reader is referred to the Web version of this article.)

north. This change contrasts with the poleward increase in zonal winds suggesting that the jet stream and surface ETC are not as strongly coupled for E_{RSI}^{sim} as they are for E_{WSI}^{sim}.

The projected changes in jet stream winds and cyclone tracks for E_{Comp}^{sim} cyclones are comparable to those of E_{WSI}^{sim}. However, the magnitude of change for jet stream winds is higher for E_{Comp}^{sim} (Fig. 2f). Furthermore, while a higher proportion of E_{Comp}^{sim} cyclone tracks in the future simulation also originate further west in the Atlantic, more propagate eastwards at more southerly latitudes and then track north-eastward over the UK (Fig. 3l). The notably higher proportion of E_{Comp}^{sim} tracks to the south in the future, compared to E_{WSI}^{sim} and E_{RSI}^{sim}, leads to higher increases in E_{Comp}^{sim} temperatures due to the combined effect of warming and a southward displacement of tracks to warmer latitudes. This is shown in Figure A2 in Appendix A using cyclone composites of 850 hPa wet bulb potential temperatures for each cyclone category. Such a southward shift in cyclone track density means a higher proportion of E_{Comp}^{sim} cyclones pass through, or form within, warmer environments that hold more moisture and latent energy, potentially leading to more rainfall and intense ETCs.

It should be noted that the projected changes are not present in each of the 12 ensemble members. As indicated by stippling in Figs. 2 and 3, the discussed changes are widespread in over half of the ensemble (7 of 12 members), in that at least 7 members agree on a positive or negative change of 20% for the zonal winds and an absolute change of 5% in the proportion of cyclone tracks. However, the level of agreement when considering at least nine members is much reduced in comparison, as indicated by the smaller area of hatching. Thus, the dynamical response is not robust across all members but occurs in more members than not.

4.2. Areas of Co-occurring wind-rain extremes

The previous section assessed ETCs that produce extreme wind footprints (E_{WSI}^{sim}) and extreme rainfall footprints (E_{RSI}^{sim}) independently as well as ETCs that produce extreme footprints of both (E_{Comp}^{sim}). In this section, we evaluate extremes that locally co-occur within the same 6-hourly period and grid cell. We assess the land area (A_{Comp}) that experiences locally co-occurring wind and rainfall extremes at least once during an ETC. A_{Comp} is grouped into the three event types E_{WSI}^{sim}, E_{RSI}^{sim}, and E_{Comp}^{sim} and presented as boxplots in Fig. 5. The number of events in each
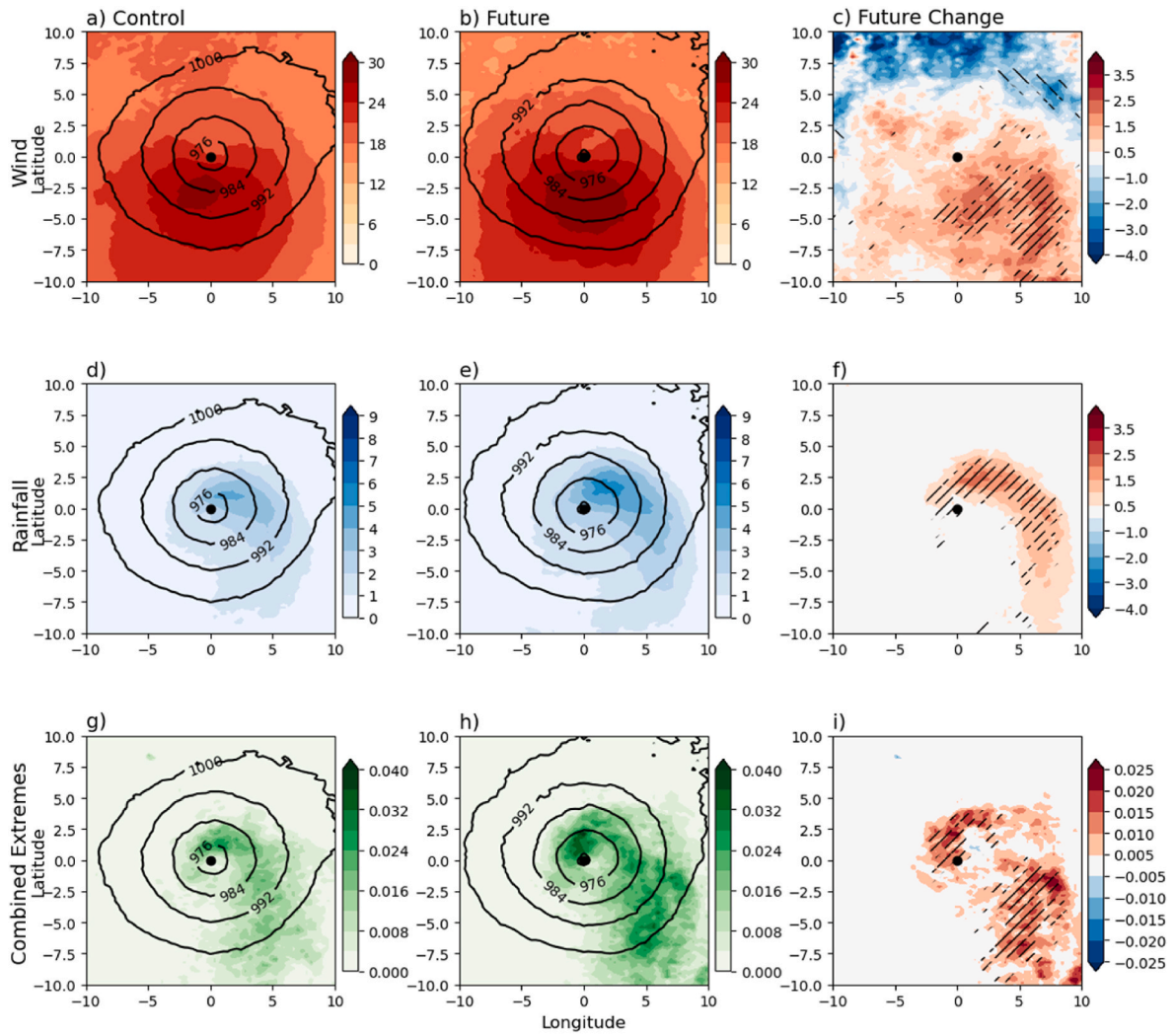
Fig. 4. ETC composites from the control (left column), future (middle column) and the future change (Future-Control; left column) produced using all E_{RSI}^{sim}, E_{WSI}^{sim}, and E_{Comp}^{sim} cyclones (440 events). Composites are provided for mean wind gusts (m s^{-1}) (top row, a-c), mean rainfall (mm) (middle row, d-f) and for the probability of locally co-occurring wind-rain extremes. Black contour lines represent the average MSLP composite. Forward (backward) hatching for future changes indicate where at least 9 members agree on a positive (negative) absolute change of 1 m s^{-1} (c), 1 mm (f), and 0.01 probability.
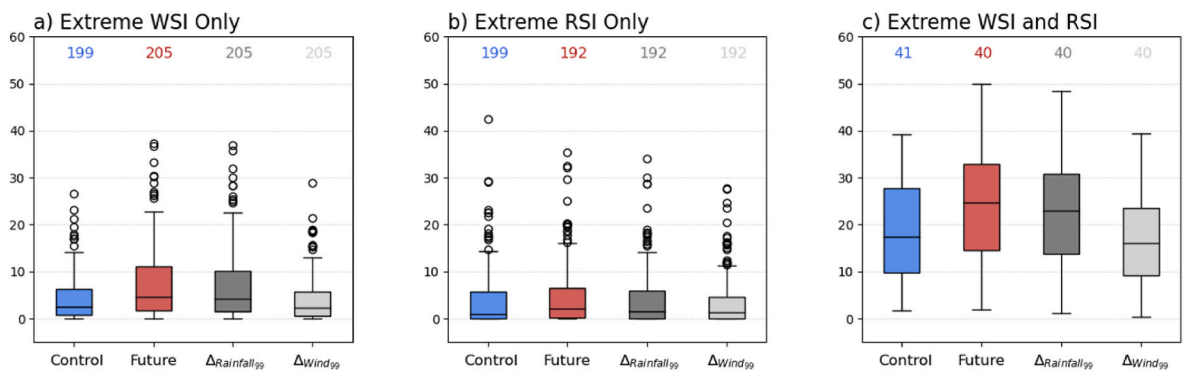

Fig. 5. The % area of land grid cells (A_{Comp}) that experience at least one 6-hourly co-occurrence of wind and rainfall above their respective 99th percentiles during a) E_{WSI}^{sim} events, b) E_{RSI}^{sim} events, and c) E_{Comp}^{sim} events. Blue and red boxplots show A_{Comp} in control and future simulations respectively, while dark and light grey boxplots show the rainfall-only and wind-only intensity-driven changes of A_{Comp} in future simulations. (For interpretation of the references to colour in this figure legend, the reader is referred to the Web version of this article.)

category is provided above each boxplot. The purpose of grouping events in this way is to illustrate the differences and similarities in A_{Comp} across the different event types.

The area of co-located extremes varies substantially across ETCs within each category; it is never larger than 50% of the ETC land area in either the control (blue boxplots) or future (red boxplots) simulations.

The largest areas are found for E_{Comp}^{sim} events meaning that these events produce extreme WSI, RSI and A_{Comp}; this might be expected given the presence of extreme WSI and RSI increases the likelihood of wind and rainfall extremes overlapping in time and space. However, comparatively large areas of co-located extremes are found in both E_{WSI}^{sim} and E_{RSI}^{sim} events, as illustrated by the number of outliers associated with the respective boxplots. This indicates that other contributing processes within ETCs, such as those related to cold and warm fronts, can lead to large areas of co-occurring extremes at the grid cell level.

By comparing boxplots from control (blue) and future (red) simulations in Fig. 5a–c, we find that A_{Comp} increases in the future simulations. This increase is found mainly for E_{WSI}^{sim} and E_{Comp}^{sim} events, with only a small increase for E_{RSI}^{sim} events. We also show boxplots of A_{Comp} in future simulations for rainfall-only (dark grey) and wind-only (light grey) intensity driven changes. These demonstrate that the increase in A_{Comp} is predominantly driven by increases in rainfall intensities. For example, the dark grey boxplot, representing the rainfall driven change, is very similar to the red boxplots from future simulations in Fig. 5a–c. In contrast, the light grey boxplot, representing the wind driven change, is almost identical to the blue boxplot from the control simulations. Thus, the increase in locally co-occurring wind-rainfall extremes is mostly driven by increased rainfall intensities.

4.3. Drivers of wind, rainfall and Co-occurring extremes within ETCs

We now characterise the drivers of wind, rainfall and their co-located extremes using temporal (Fig. 6) and spatial composites (Figs. 4 and 7). The temporal composites demonstrate the evolution of the WSI, RSI and area of local co-occurring extremes during the lifetime of an ETC. Also shown are the contributions of the frontal and non-frontal sectors during this lifecycle. The spatial composites demonstrate where the highest wind and rainfall intensities occur, as well as where the highest frequencies of co-located extremes occur, relative to the centre of the ETC. Combining these, we build a picture of the components within ETCs that cause wind, rainfall, and co-located extremes.

The RSI metric peaks before an ETC reaches its maximum vorticity and rainfall extremes largely occur close to a warm front or within an area where cold and warm fronts overlap (Fig. 6a). Spatially, the highest rainfall totals occur to the east of the ETC centre, particularly the northeast (Fig. 4d and e); likely associated with warm and cold fronts as well as with the ascent of the WCB. In contrast, the WSI metric peaks after the peak in maximum vorticity and is predominantly driven by non-frontal processes in the ETC cold sector, following the passage of the cold front (Fig. 6b). The highest winds occur south of the ETC centre where wind directions align with the direction of the ETC and where the strongest surface winds of cold conveyor belts and sting jets are generally found.

The area of co-located wind and rainfall extremes within ETCs generally peaks at the same time as the peak in maximum vorticity, after the peak in RSI and before the peak in WSI. We find that locally co-occurring wind-rainfall extremes largely occur close to the warm front or where cold and warm frontal areas overlap (Fig. 6c). Spatially, there are two areas with high frequencies of co-occurring extremes. One is to the east of the ETC centre between the wind maxima to the west and rainfall maxima to the east (Fig. 4 g, h), and the second is to the north of the ETC centre in both control and future simulations.

We further explore the drivers of high frequencies of co-occurring wind-rainfall extremes in Fig. 7. Here, we present the frequency of co-occurring extremes within each frontal and non-frontal feature, alongside red and blue contours which represent where a high frequency of cold and warm fronts are detected at the time a cyclone reaches its maximum vorticity (i.e. t = 0 in Fig. 6). We choose to show the contours at t = 0 as the position of fronts relative to the ETC centre changes throughout the life cycle, and the highest frequencies in co-occurring extremes are found at this time.

The position of fronts is largely what we expect, with some exception. Warm fronts extend from the ETC centre to the east and southeast (Fig. 7a and b). Cold fronts are mainly situated in two separate locations (Fig. 7g and h) and, interestingly, their structure suggests the presence of ETCs that follow the Shapiro-Keyser conceptual model. The first cold front location close to the ETC centre on the western side indicates the presence of a bent back front arising from the cold conveyor belt wrapping around the ETC centre. However, from the Shapiro-Keyser conceptual model, we would expect to see a bent-back warm front. This discrepancy is likely an issue with how the algorithm differentiates between warm and cold fronts, but the result still indicates the presence of a bent back front that separates warm air in the cyclone core from the colder surrounding air. The second cold front location to the southeast, detached from the centre, indicates the presence of a frontal fracture that is typical of a Shapiro-Keyser cyclone.

The highest frequencies of locally co-occurring wind and rainfall extremes associated with each frontal feature naturally overlap with contours indicating a high frequency of fronts. Warm fronts largely drive co-occurring extremes to the east of the ETC centre over a wide area (Fig. 7a and b) whilst the cold front drives co-located extremes close to the ETC centre on the western side and further away to the southeast (Fig. 7g and h). Frequencies are generally smaller for cold fronts and cover a narrower area than those associated with warm fronts. For warm and cold front overlaps, a wide area of high frequencies is found southeast of the ETC centre, similar to warm fronts. Equally, similar to cold fronts, a confined area of relatively higher frequencies is seen just north of the ETC centre. This frequency is notably higher than that seen for cold fronts alone just west of the ETC centre, indicating that the
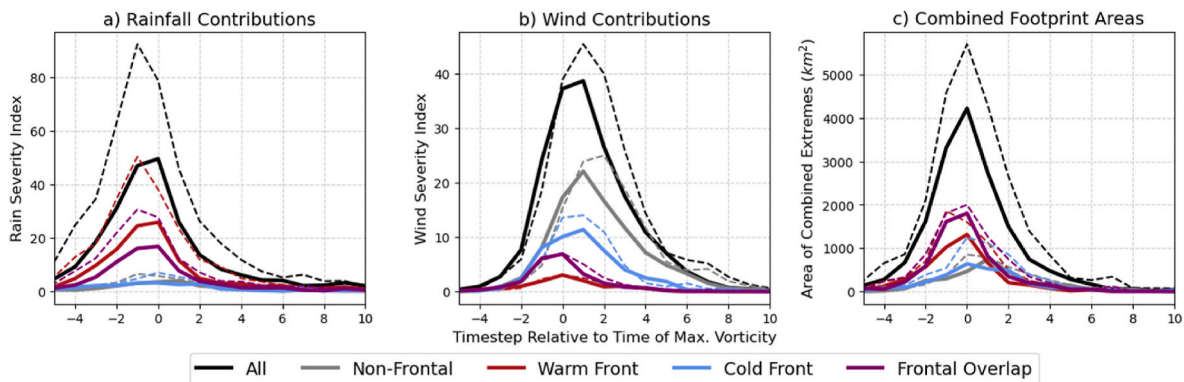

Fig. 6. Temporal composites of a) RSI, b) WSI, and c) combined footprint areas in all E_{RSI}^{sim}, E_{WSI}^{sim}, and E_{Comp}^{sim} cyclones (440 events). Solid lines represent the control simulations while dashed lines represent the future simulations. The contributions of the frontal and non-frontal areas are also provided. To produce composites, ETCs are centred at the time of maximum vorticity (timestep = 0).
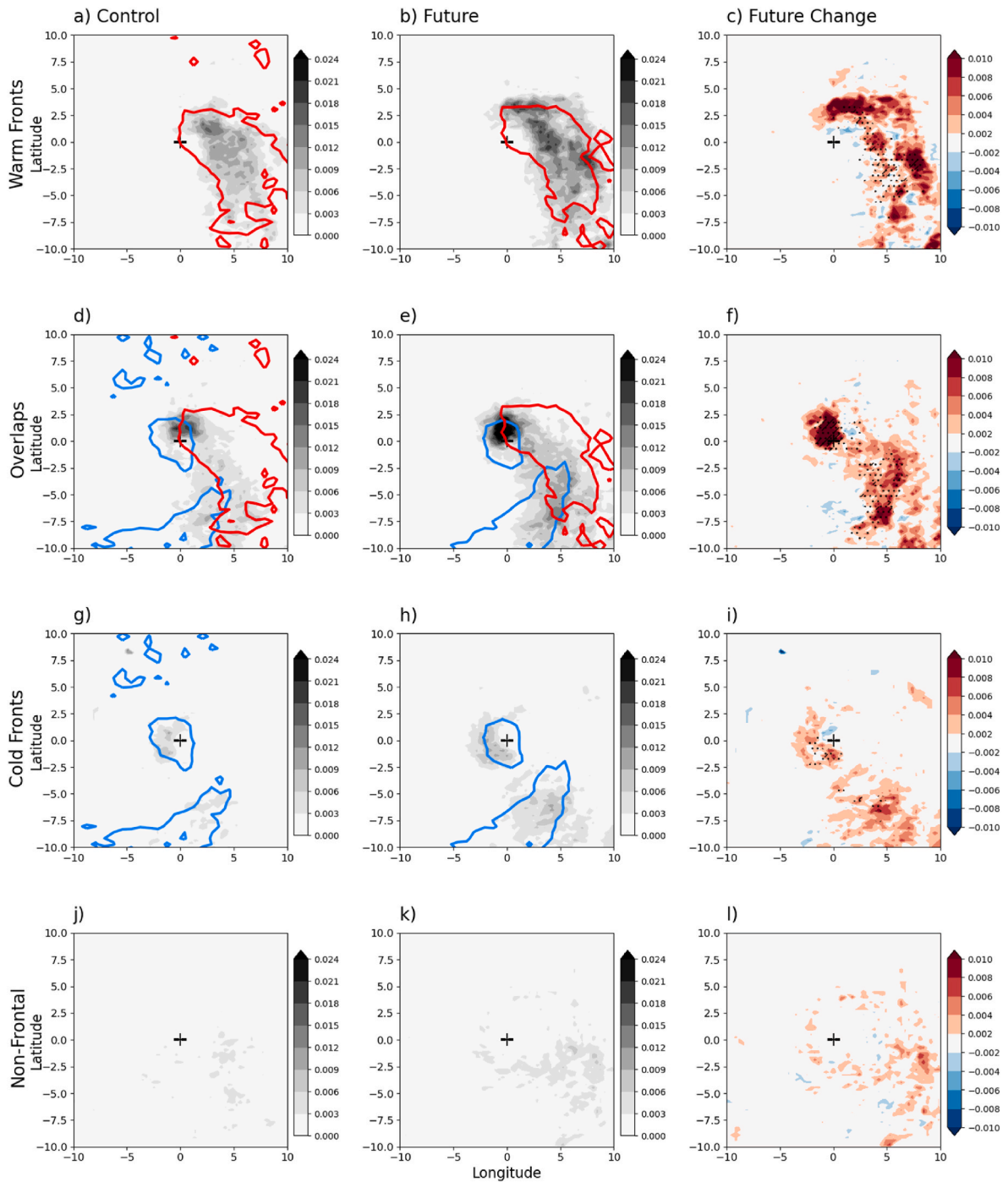
Fig. 7. The probability of locally co-occurring extremes within warm fronts (top row, a-c), areas where warm and cold fronts overlap (second row, d-f), cold fronts (third row, g-i) and non-frontal areas (bottom row, j-l). Probabilities are estimated for events where either the WSI or RSI 1-year RL is exceeded (i.e. E^{sim}_{WSI}, E^{sim}_{RSI} and E^{sim}_{Comp}) and presented for the control (left column) and future (middle column) simulations as well as their future change (Future – Control). Red and blue contours indicate the areas where warm and cold fronts are frequently detected (>10 % of timesteps). Black crosses indicate the centre of an ETC. Hatching (stippling) for future changes indicates where at least 9 (7) members agree on a positive change of 0.004 (no agreement found on negative change). (For interpretation of the references to colour in this figure legend, the reader is referred to the Web version of this article.)

combination of processes related to cold fronts and warm fronts may yield a higher frequency of combined extremes than either alone.

4.4. Drivers of future changes in Co-occurring extremes within ETCs

The temporal evolutions of RSI and WSI in the future simulations are similar to the control, though intensified by comparison (Fig. 6). Rainfall extremes are amplified within each of the frontal and non-frontal features throughout the lifecycle of future ETCs (Fig. 6a). This result suggests that extreme rainfall thresholds are exceeded earlier and later in ETCs, potentially causing longer duration extremes over land. In the ETC composites, we find that rainfall is increased over areas where high rainfall occurs in the control although the highest increases in mean rainfall (Fig. 4f) are not co-located with the highest values in the control (Fig. 4d), indicating an increase in the area of high rainfall.

Winds are also higher in both the temporal and spatial future

composites. In the temporal composites, wind increases are seen only from the point at which ETCs reach their maximum vorticity onwards (Fig. 6b), with the largest change for winds within the cold front (compare blue dashed and solid lines). Changes after this point are dominated by non-frontal areas within the cold sector. Similarly to rainfall, the highest changes to mean wind gusts (Fig. 4c) are not co-located with the highest values in the control (Fig. 4a), indicating that future wind footprints are larger.

Locally co-occurring extremes also increase in frequency in the future simulations. The temporal composites show an increase that largely follows that of rainfall-only; co-occurring extremes are more frequent throughout the temporal evolution of an ETC, leading to more co-occurrences earlier and later in its lifecycle (Fig. 6c). This further highlights the influence of increasing rainfall intensities on increases in co-occurring extremes. However, the spatial composites for co-occurring extremes (Fig. 4i) show a different spatial signature to those for rainfall (Fig. 4f); increases in co-occurring extremes are widespread, with the highest increases occurring west and southeast of the ETC centre. The future changes in wind, rainfall and co-occurring extremes are seen across the ensemble with at least 9 of 12 members in agreement on a positive increase greater than 1 m s^{-1}, 1 mm, and a probability of 0.01 respectively (Fig. 4c–f,i).

Increases in co-occurring extremes are found within frontal and non-frontal areas (compare the solid and dashed lines of the temporal composites in Fig. 6c). These changes are quantified in Table 2 which provides changes to the total frequency of co-occurring extremes within each frontal area, as well as its relative percentage contribution. The largest increase in frequency of 80% is found near the cold front, which increases its relative percentage contribution from 18% in the control to 22% in the future. This indicates that processes within the cold front become relatively more important for co-occurring extremes in the future simulations. Spatially, the largest absolute increases in the cyclone composites are generally located close to where the highest frequencies are found in the control for each frontal area. Within overlapping frontal areas, the largest increases are found closer to areas with high frequencies of cold fronts than those for warm fronts (Fig. 7f), that is, on the western side of the ETC centre and further to the southeast (Fig. 7d and e), suggesting that changes in overlapping frontal areas are mainly driven by processes related to the cold fronts. The agreement between ensemble members on the future increases is lower within frontal areas compared to the general change in local co-occurrences (Fig. 4i). Agreement between at least 9 members is limited to a confined area northwest of the cyclone centre (Fig. 7f - hatching), while agreement between at least 7 members is widespread for each frontal area (Fig. 7c–f,i - stippling).

Table 2

Frontal and non-frontal relative contributions to the total frequency of locally co-occurring extremes in control and future climate simulations along with future change in these contributions (first three rows). Contributions are calculated as the percentage of co-occurring extremes that occur within a feature. Also provided in the last row is the future change in total frequency of co-occurring extremes within each feature separately.

	Warm Front	Frontal Overlaps	Cold Front	Non-Frontal
% Change in Total Frequency	53.26	31.56	80.02	36.44
Control Relative Contribution	27.44	36.50	18.11	17.94
Future Relative Contribution	28.58	32.63	22.16	16.63
% Change in Relative Contribution	4.14	−10.60	22.32	−7.29

5. Discussion and conclusions

This paper has assessed compound wind and rainfall extremes, produced by extra-tropical cyclones (ETCs), and their future projections within a 12-member ensemble of 2.2 km convection-permitting climate model simulations over the UK following the RCP8.5 high emissions scenario. Compound extremes were assessed from two perspectives: 1) we quantified the likelihood of ETCs that produce extremely severe wind and rainfall footprints in the same event and identified the jet stream and cyclone track characteristics of these events; 2) we assessed areas of locally co-occurring 6-hourly extremes of wind and rainfall within ETCs, and evaluated the contribution from their frontal and non-frontal drivers. In doing so, we identified thermodynamical and dynamical sources of future changes in these compound extremes.

5.1. Extreme wind and rainfall footprints (WSI and RSI)

The most extreme wind and rainfall footprints, WSI and RSI respectively, have contrasting jet stream characteristics. WSI extremes are favoured by a strong jet stream that intensifies ETCs and associated winds, while RSI extremes are favoured by a weak jet and slow moving ETCs that allow rainfall to persist over localities for longer durations. However, a strong jet is not a limiting factor for extreme RSI as our results indicate that ETCs with both WSI and RSI extremes require a strong jet stream. Compound extremes are also more likely under a southerly jet stream that carries an ETC over warmer regions than normal (e.g. 30-40° latitude) bringing more intense rainfall, in line with Clausius-Clapeyron, and higher wind speeds due to the additional latent heat energy that can intensify ETCs. The area of land affected by wind and rainfall extremes in the UK and Ireland is then maximised if the centre of the ETC tracks over the centre of the land mass. This is because the highest winds occur southward of the ETC centre while the highest 6-hourly rainfall intensities occur north-eastward of the cyclone centre.

Climate simulations project an increased frequency of ETCs that produce extreme WSI and RSI in the same storm. The bivariate return period for a joint exceedance of the 2-year return levels of WSI and RSI, defined from the control, reduces from once every 18 years in the control to once every 5 years in the future, a 3.6-fold increase in frequency. This change is largely explained by increased RSI, pointing to a predominantly thermodynamic response, while an increase in WSI accounts for a small fraction of the change. The results largely agree with previous studies. In the 12 km model that drives the 2.2 km simulations assessed here, Bloomfield et al. (2023) find a similar 3-fold future increase in the frequency of windstorms co-occurring with severe flooding. Furthermore, CMIP6 models project an increase in daily co-occurrences of wind and rain above their 99th percentiles, although models vary in their magnitude of change (Ridder et al., 2022; François and Vrac, 2023), while increasing precipitation is the main driver of projected increases in the co-occurrence of storm surge and heavy precipitation in coastal areas (Bevacqua et al., 2019; 2020a).

The results also indicate important contributions from changes in ETC tracks and the jet stream to the future increase in WSI and RSI. The increased WSI is likely a result of the strengthened jet stream in future events, as well as increased diabatic contributions to ETC intensification indicated by the local poleward deflection of ETC tracks close to the UK (Tamarin-Brodsky and Kaspi, 2017). Furthermore, a southward displaced jet stream within future events with WSI and RSI extremes causes ETCs to propagate through more southerly and warmer latitudes causing a dynamically enhanced increase in temperature which may further intensify RSI and WSI. This southward displacement of cyclone tracks and jet stream for extreme events (E_{Comp}^{sim}; E_{WSI}^{sim}) conflicts with the changes seen for all ETCs. On average, the simulations project ETC tracks to have an eastward extension over Europe, in line with CMIP5 and CMIP6 models (Zappa et al., 2013; Priestley and Catto, 2022a), and a moderately strengthened jet stream with no change in position. The southward

displacement further conflicts with the average response of the jet stream in CMIP6 models who mostly project a poleward shift in average jet position with varying magnitude that can depend on a model's ability to represent important feedbacks from drivers such as tropical warming and Arctic amplification (Screen et al., 2022; Woollings et al., 2023). While such changes in mean circulation may have implications for extremes, the link to extremes may not be straightforward. Our results show that changes to jet stream and ETC track characteristics are different between extremes and non-extremes. Hence, diagnosing the effect of large-scale dynamical changes on extreme weather requires assessment of circulation changes specific to extreme events.

5.2. Local co-occurrence of 6-hourly wind-rainfall extremes

Large areas of locally co-occurring wind-rainfall extremes are most likely to occur in ETCs where both WSI and RSI are extreme, however, similar areas occur in ETCs where only WSI or RSI are extreme, highlighting the presence of contributing processes within ETCs besides those causing WSI or RSI extremes. Local wind and rainfall extremes, defined as local 99th percentile exceedances, are driven by mostly separate processes within ETCs that occur at different times in their lifecycle and in different locations relative to the ETC centre (Bengtsson et al., 2009). Rainfall extremes peak prior to an ETC's maximum intensity caused by ascending air over fronts and convection. Wind extremes peak at the time of maximum ETC intensity caused by tight pressure gradients and jet features. The highest frequency of co-occurring extremes is found at the times and locations where these separate drivers coincide; near the time of maximum ETC intensity to the north, east and southeast of the ETC centre. The highest frequency occurs north of the ETC centre, likely due to rainfall from the ascending warm conveyor belt (WCB) over areas of high winds due to a westward moving cold conveyor belt (CCB) (Schultz, 2001). Latent heating during WCB ascent can also amplify winds in the CCB (Schemm and Wernli, 2014). To the east, co-occurrences can arise due to frontal rainfall coinciding with high winds from tight pressure gradients as well as due to shared drivers such as the WCB (Hewson and Neu, 2015) and convection along cold fronts (Ludwig et al., 2015; Eisenstein et al., 2022), though the latter has a relatively small contribution.

The climate simulations project an increase in the land area experiencing a joint exceedance of wind and rainfall above their respective 99th percentiles, mostly due to increased rainfall intensities within fronts. The relative contributions from fronts, and their importance, to co-occurring extremes are generally consistent between control and future climates, although the absolute contribution from cold fronts increases relative to warm fronts, possibly arising from an increase in convection along the cold front (Berthou et al., 2022). It is important to note that the identified drivers of locally co-occurring extremes, such as the CCB, WCB and convection, are poorly represented in coarse-resolution models (Priestley and Catto, 2022b; Manning et al., 2023; Prein et al., 2015), while even state-of-the-art reanalysis products such as ERA5 can be unreliable for co-occurring extremes (Zscheischler et al., 2021). This raises questions over the reliability of coarse resolution models and the results highlight the need for process-oriented evaluations of such models and comparisons with high-resolution counterparts.

5.3. Summary

This study has quantified future changes in compound wind-rain extremes and revealed important contributions from large-scale factors (jet stream, cyclone track) as well as frontal and non-frontal drivers within ETCs. In a warmer climate, ETCs are more likely to produce severe footprints of extreme winds (WSI) and rainfall (RSI) in the same event, while the area of locally co-occurring wind-rainfall extremes will also increase. Such increases will have implications for impacts: increased WSI-RSI extremes may lead to more windstorms co-occurring

with flood events (Bloomfield et al., 2023, 2024) that could cause larger aggregations of separate impacts throughout the UK to industries such as rail transport (e.g. Hillier et al., 2015, 2020), while both may combine in a single catchment over the lifetime of a storm to enhance coastal compound flooding (Bevacqua et al., 2017; Ward et al., 2018). Impacts due to local co-occurring extremes are less understood or remain largely anecdotal, though their increased frequency may hasten the deterioration of buildings (Jeong et al., 2020).

Increased rainfall is the main cause of the projected change in compound wind-rain extremes, though a strengthened jet stream and a southward displacement in its position likely contributes to this projected increase. The thermodynamic-driven change in rainfall is a robust feature of the future climate projected by climate models (O'Gorman and Schneider, 2009). However, the large-scale changes are not seen across all ensemble members assessed here and there is generally less confidence in the magnitude of climate-induced atmospheric circulation changes (Shepherd, 2014) such as changes to cyclone tracks (Chang et al., 2012; Harvey et al., 2015) and the jet stream (Harvey et al., 2023). The use of a single model is therefore a weakness in this study.

Despite the uncertainty of the dynamical response, our results demonstrate the influence that such large-scale changes can have on compound extremes and can be considered a type of storyline conditional on the warming scenario and jet stream response (Zappa, 2019). For example, a stronger/weaker response of the jet stream and cyclone tracks in future climate simulations may bring larger/smaller changes in the probability of joint extremes. Equally, a lower emissions scenario, compared to the high emissions RCP8.5 scenario used here, may bring a smaller increase in rainfall extremes as well as a weaker intensification to cyclones (Priestley and Catto, 2022a,b). Going forward, the results offer a starting point for process-oriented analyses of compound wind-rainfall extremes.

CRediT authorship contribution statement

Colin Manning: Writing – review & editing, Writing – original draft, Visualization, Methodology, Formal analysis, Conceptualization. **Elizabeth J. Kendon:** Writing – review & editing, Supervision, Methodology, Conceptualization. **Hayley J. Fowler:** Writing – review & editing, Supervision, Project administration, Methodology, Funding acquisition, Conceptualization. **Jennifer L. Catto:** Writing – review & editing, Supervision, Methodology, Funding acquisition, Conceptualization. **Steven C. Chan:** Writing – review & editing, Formal analysis. **Philip G. Sansom:** Methodology.

Declaration of competing interest

The authors declare that they have no known competing financial interests or personal relationships that could have appeared to influence the work reported in this paper.

Data availability

Wind and rainfall data is freely available. Other data can be made available upon reasonable request.

Acknowledgements
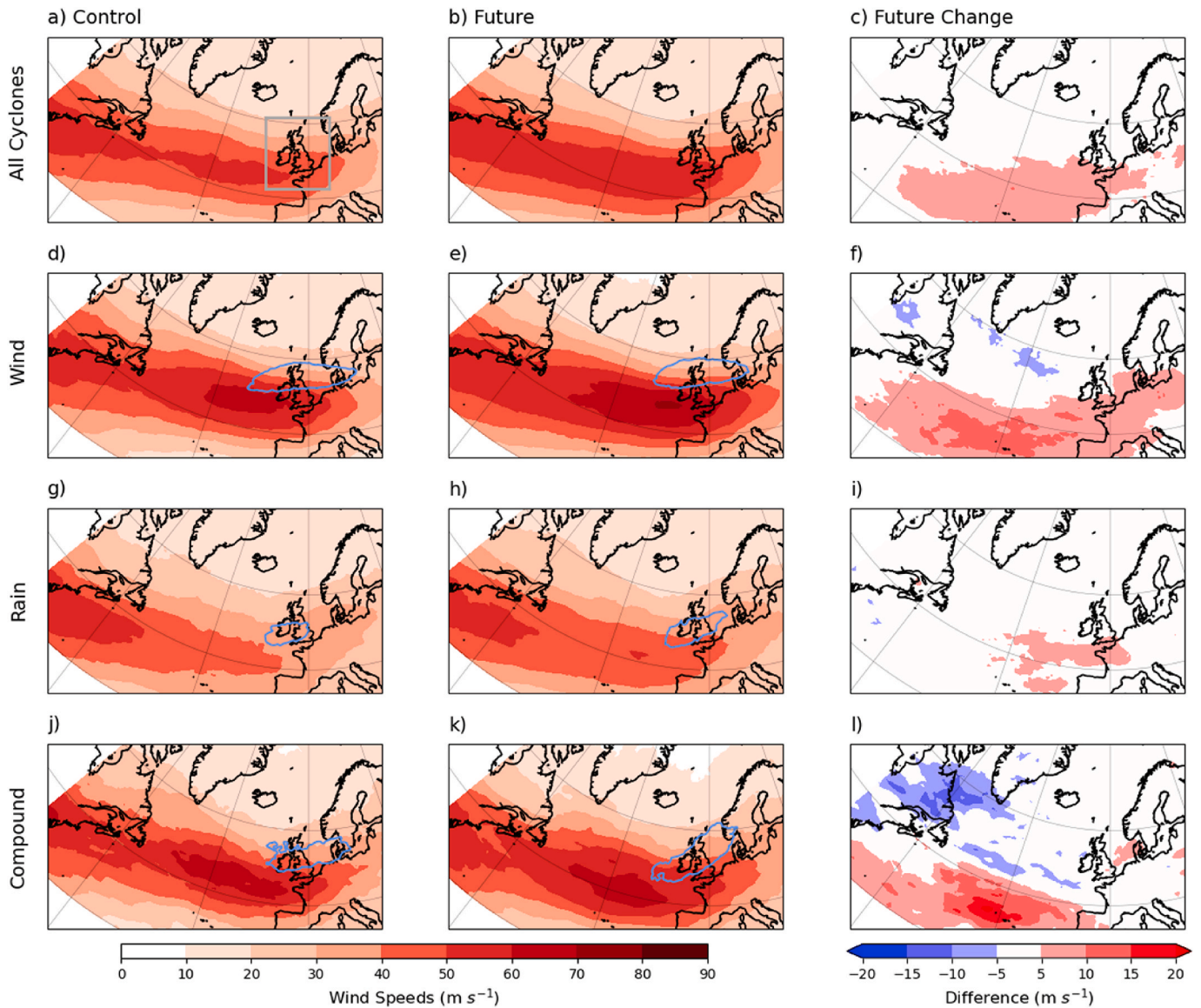
Appendix A. Additional Figures

Fig. A1. Average 300 hPa wind speeds for ETCs from the Control (left column), Future (middle column) and future change (Future – Control). Wind speeds and their future change are provided for all cyclones (top row – a-c) as well as cyclones for the three event types E_{WSI}^{sim} (Extreme WSI only – d-f), E_{RSI}^{sim} (Extreme RSI only – g-i), and E_{Comp}^{sim} (compound extremes – j-l). Blue contour lines in panels d–e, g-h, and j-k represent the 50% frequency contour of the track density from Fig. 3 associated with the given ETC type. Grey box in panel (a) represents CPM domain boundaries.
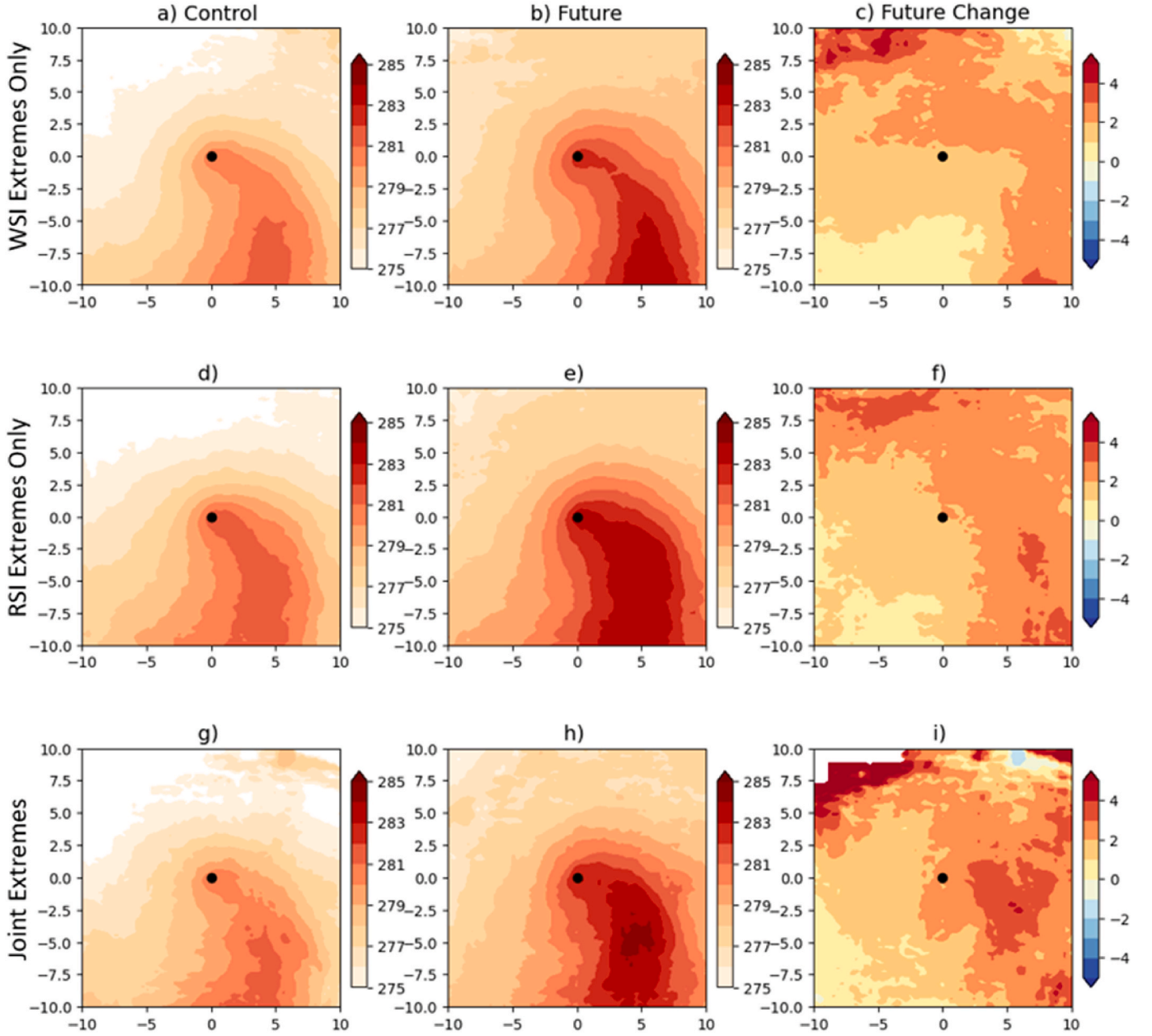
Fig. A2. Cyclone composites of ϑ_W at 850 hPa in control (left column) and future (middle column) simulations as well as the future change (future-control, right column). Composites are provided for the three event types E_{WSI}^{sim} (Extreme WSI only – a-c), E_{RSI}^{sim} (Extreme RSI only – d-f), and E_{Comp}^{sim} (Both extremes – g-i).

Appendix B. Methods Appendix

B.1. Fitting Bivariate Statistical Model

Bivariate return periods are estimated through a peak-over-threshold approach in which a parametric copula-based probability distribution is applied to events WSI^{bi} and RSI^{bi}, which refer to events where both WSI and RSI exceed their respective 95th percentiles. The 95th percentiles are defined from the control simulation and are demonstrated by the solid horizontal and vertical black lines in Fig. 2a and b. A copula is a multivariate distribution function that models the dependence between random variables independently of the marginal (univariate) distributions. According to Sklar (1959), the joint distribution function (F) of WSI^{bi} and RSI^{bi} may be written as:

$$F\left(WSI^{bi}, RSI^{bi}\right) = C(u_{WSI^{bi}}, u_{RSI^{bi}}), \tag{3}$$

where C is the copula modelling the dependence between the WSI^{bi} and RSI^{bi} pairs that jointly exceed their respective 95th percentiles, while $u_{WSI^{bi}} = F_{WSI^{bi}}(WSI^{bi})$ and $u_{RSI^{bi}} = F_{RSI^{bi}}(RSI^{bi})$ are uniformly distributed cumulative probabilities on [0,1]. $F_{WSI^{bi}}$ and $F_{RSI^{bi}}$ are then the univariate cumulative distribution functions of WSI^{bi} and RSI^{bi} respectively and are modelled using a GPD. The copula instead is fit to $u_{WSI_{bi}}^{emp}$ and $u_{RSI_{bi}}^{emp}$ which were obtained via empirical CDF to avoid errors introduced by potential misspecification of the parameters of the marginal distributions ($F_{WSI^{bi}}$ and $F_{RSI^{bi}}$). A range of

copula families, each with their own individual dependence properties, may be chosen to represent the dependence between WSI^{bi} and RSI^{bi}. Using the R package Vine Copula, we selected the highest ranked of the following families according to the Akaike information criterion (AIC): Gaussian, t, Clayton, Gumbel, Frank, Joe, BB1 BB6, BB7, and BB8. In both the control and future simulation, this resulted in the Clayton copula being selected.

B.2. Estimate contributions to changes in Bivariate Return Periods

We estimate how bivariate return periods would change in the future simulations when only taking into account the change with respect to the control of (1) the wind severity index (WSI) distribution (all values without conditioning on the rainfall severity index (RSI)), (2) the WSI distribution (all values without conditioning on RSI), and (3) the dependence between WSI and RSI. The bivariate RP for each case is estimated following equation (3) as follows.

Experiment (1)   From WSI in the control simulation (WSI^{Ctrl}), we calculate the associated empirical CDF to obtain $U_{WSI^{Ctrl}}$. From WSI in the future simulation (WSI^{Fut}), we define the empirical CDF $F_{WSI^{Fut}}$ that is used to obtain $WSI_1 = F_{WSI^{Fut}}^{-1}(U_{WSI^{Ctrl}})$. We then compute the bivariate RP using the bivariate model fit to (WSI_1, RSI^{Ctrl}) that jointly exceed the respective 95th percentiles of WSI^{Ctrl} and RSI^{Ctrl}, where RSI^{Ctrl} is RSI from the control simulation. The variables (WSI_1, RSI^{Ctrl}) have the same Spearman correlations and tail dependence as during the control but the univariate distribution of WSI_1 is that from the future.

Experiment (2)   Similar to experiment (1) but swapping WSI and RSI.

Experiment (3)   With variables ($WSI^{Ctrl}; RSI^{Ctrl}$), we obtain their respective empirical CDFs from which we define $WSI_3 = F_{WSI^{Ctrl}}^{-1}(U_{WSI^{Fut}})$ and $RSI_3 = F_{RSI^{Ctrl}}^{-1}(U_{RSI^{Fut}})$. The variables ($WSI_3, RSI_3$) then have the same Spearman correlation and tail dependence as ($WSI^{Fut}; RSI^{Fut}$), but the univariate distributions are those from the control simulations. We then compute the bivariate RP using the bivariate model fit to the pairs (WSI_3, RSI_3) that jointly exceed the 95th percentiles of ($WSI^{Ctrl}; RSI^{Ctrl}$).

References

Bengtsson, L., Hodges, K.I., Esch, M., Keenlyside, N., Kornblueh, L., Luo, J.J., Yamagata, T., 2007. How may tropical cyclones change in a warmer climate? Tellus 59 (4), 539–561.

Bengtsson, L., Hodges, K.I., Keenlyside, N., 2009. Will extratropical storms intensify in a warmer climate? J. Clim. 22 (9), 2276–2301.

Berthou, S., Roberts, M.J., Vannière, B., Ban, N., Belušić, D., Caillaud, C., Crocker, T., de Vries, H., Dobler, A., Harris, D., Kendon, E.J., 2022. Convection in future winter storms over Northern Europe. Environ. Res. Lett. 17 (11), 114055.

Berry, G., Reeder, M.J., Jakob, C., 2011. A global climatology of atmospheric fronts. Geophys. Res. Lett. 38 (4).

Bevacqua, E., Maraun, D., Hobæk Haff, I., Widmann, M., Vrac, M., 2017. Multivariate statistical modelling of compound events via pair-copula constructions: analysis of floods in Ravenna (Italy). Hydrol. Earth Syst. Sci. 21 (6), 2701–2723.

Bevacqua, E., Maraun, D., Vousdoukas, M.I., Voukouvalas, E., Vrac, M., Mentaschi, L., Widmann, M., 2019. Higher probability of compound flooding from precipitation and storm surge in Europe under anthropogenic climate change. Sci. Adv. 5 (9), eaaw5531.

Bevacqua, E., Vousdoukas, M.I., Zappa, G., Hodges, K., Shepherd, T.G., Maraun, D., Mentaschi, L., Feyen, L., 2020a. More meteorological events that drive compound coastal flooding are projected under climate change. Communications earth & environment 1 (1), 47.

Bevacqua, E., Zappa, G., Shepherd, T.G., 2020b. Shorter cyclone clusters modulate changes in European wintertime precipitation extremes. Environ. Res. Lett. 15 (12), 124005.

Bloomfield, H.C., Hillier, J., Griffin, A., Kay, A.L., Shaffrey, L.C., Pianosi, F., James, R., Kumar, D., Champion, A., Bates, P.D., 2023. Co-occurring wintertime flooding and extreme wind over Europe, from daily to seasonal timescales. Weather Clim. Extrem. 39, 100550.

Bloomfield, H.C., Bates, P., Shaffrey, L.C., Hillier, J., Champion, A., Cotterill, D., Pope, J. O., Kumar, D., 2024. Synoptic conditions conducive for compound wind-flood events in Great Britain in present and future climates. Environ. Res. Lett. 19 (2), 024019.

Catto, J.L., Shaffrey, L.C., Hodges, K.I., 2010. Can climate models capture the structure of extratropical cyclones? J. Clim. 23 (7), 1621–1635.

Catto, J.L., Pfahl, S., 2013. The importance of fronts for extreme precipitation. J. Geophys. Res. Atmos. 118 (19), 10–791.

Catto, J.L., Madonna, E., Joos, H., Rudeva, I., Simmonds, I., 2015. Global relationship between fronts and warm conveyor belts and the impact on extreme precipitation. J. Clim. 28 (21), 8411–8429.

Catto, J.L., Ackerley, D., Booth, J.F., Champion, A.J., Colle, B.A., Pfahl, S., Pinto, J.G., Quinting, J.F., Seiler, C., 2019. The future of midlatitude cyclones. Curr. Clim. Change Rep. 5, 407–420.

Catto, J.L., Dowdy, A., 2021. Understanding compound hazards from a weather system perspective. Weather Clim. Extrem. 32, 100313.

Chan, S.C., Kendon, E.J., Fowler, H.J., Blenkinsop, S., Roberts, N.M., Ferro, C.A.T., 2014. The value of high-resolution Met Office regional climate models in the simulation of multi-hourly precipitation extremes. J Climate 27 (16), 6155–6174. https://doi.org/10.1175/JCLIM-13-00723.1.

Chang, E.K., Guo, Y., Xia, X., 2012. CMIP5 multimodel ensemble projection of storm track change under global warming. J. Geophys. Res. Atmos. 117 (D23).

Couasnon, A., Eilander, D., Muis, S., Veldkamp, T.I., Haigh, I.D., Wahl, T., Winsemius, H. C., Ward, P.J., 2020. Measuring compound flood potential from river discharge and storm surge extremes at the global scale. Nat. Hazards Earth Syst. Sci. 20 (2), 489–504.

Dacre, H.F., Hawcroft, M.K., Stringer, M.A., Hodges, K.I., 2012. An extratropical cyclone atlas: a tool for illustrating cyclone structure and evolution characteristics. Bull. Am. Meteorol. Soc. 93 (10), 1497–1502.

Dawkins, L.C., Stephenson, D.B., 2018. Quantification of extremal dependence in spatial natural hazard footprints: independence of windstorm gust speeds and its impact on aggregate losses. Nat. Hazards Earth Syst. Sci. 18 (11), 2933–2949.

De Luca, P., Messori, G., Pons, F.M., Faranda, D., 2020. Dynamical systems theory sheds new light on compound climate extremes in Europe and Eastern North America. Q. J. R. Meteorol. Soc. 146 (729), 1636–1650.

Earl, N., Dorling, S., Starks, M., Finch, R., 2017. Subsynoptic-scale features associated with extreme surface gusts in UK extratropical cyclone events. Geophys. Res. Lett. 44 (8), 3932–3940.

Earl, N., Simmonds, I., 2019. Sub synoptic scale features of the South Australia Storm of September 2016–Part II: analysis of mechanisms driving the gusts. Weather 74 (9), 301–307.

Eisenstein, L., Schulz, B., Qadir, G.A., Pinto, J.G., Knippertz, P., 2022. Identification of high-wind features within extratropical cyclones using a probabilistic random forest–Part 1: Method and case studies. Weather and Climate Dynamics 3 (4), 1157–1182.

François, B., Vrac, M., 2023. Time of emergence of compound events: contribution of univariate and dependence properties. Nat. Hazards Earth Syst. Sci. 23 (1), 21–44.

Gentile, E.S., Gray, S.L., 2023. Attribution of observed extreme marine wind speeds and associated hazards to midlatitude cyclone conveyor belt jets near the British Isles. Int. J. Climatol. 43 (6), 2735–2753.

Gholamalipour, P., Ge, H., Stathopoulos, T., 2022. Wind-driven rain (WDR) loading on building facades: a state-of-the-art review. Build. Environ. 221, 109314.

Hart, N.C., Gray, S.L., Clark, P.A., 2017. Sting-jet windstorms over the North Atlantic: climatology and contribution to extreme wind risk. J. Clim. 30 (14), 5455–5471.

Harvey, B.J., Shaffrey, L.C., Woollings, T., 2015. Deconstructing the climate change response of the Northern Hemisphere wintertime storm tracks. Clim. Dynam. 45, 2847–2860.

Harvey, B., Hawkins, E., Sutton, R., 2023. Storylines for future changes of the North Atlantic jet and associated impacts on the UK. Int. J. Climatol. 43 (10), 4424–4441.

Hénin, R., Ramos, A.M., Pinto, J.G., Liberato, M.L., 2021. A ranking of concurrent precipitation and wind events for the Iberian Peninsula. Int. J. Climatol. 41 (2), 1421–1437.

Hewson, T.D., 1998. Objective fronts. Meteorol. Appl. 5 (1), 37–65.

Hewson, T.D., Neu, U., 2015. Cyclones, windstorms and the IMILAST project. Tellus Dyn. Meteorol. Oceanogr. 67 (1), 27128.

Hillier, J.K., Macdonald, N., Leckebusch, G.C., Stavrinides, A., 2015. Interactions between apparently 'primary' weather-driven hazards and their cost. Environ. Res. Lett. 10 (10), 104003.

Hillier, J.K., Matthews, T., Wilby, R.L., Murphy, C., 2020. Multi-hazard dependencies can increase or decrease risk. Nat. Clim. Change 10 (7), 595–598.

Hillier, J.K., Dixon, R.S., 2020. Seasonal impact-based mapping of compound hazards. Environ. Res. Lett. 15 (11), 114013.

Hoskins, B.J., Hodges, K.I., 2002. New perspectives on the Northern Hemisphere winter storm tracks. J. Atmos. Sci. 59 (6), 1041–1061.

Jeong, D.I., Cannon, A.J., Morris, R.J., 2020. Projected changes to wind loads coinciding with rainfall for building design in Canada based on an ensemble of Canadian regional climate model simulations. Climatic Change 162, 821–835.

Kendon, M., McCarthy, M., 2015. The UK's wet and stormy winter of 2013/2014. Weather 70 (2), 40–47.

Kendon, E.J., Short, C., Pope, J., Chan, S., Wilkinson, J., Tucker, S., Bett, P., Harris, G., Murphy, J., 2021a. Update to UKCP Local (2.2 Km) Projections. Met Office Hadley Centre, Exeter, UK.

Kendon, E.J., Prein, A.F., Senior, C.A., Stirling, A., 2021b. Challenges and outlook for convection-permitting climate modelling. Phil. Trans. R. Soc. A 20190547. https://doi.org/10.1098/rsta.2019.0547.

Kendon, E.J., Fischer, E., Short, C.J., 2023. Variability conceals emerging trend in 100yr projections of UK local hourly rainfall extremes. Nature Comms. https://doi.org/10.1038/s41467-023-36499-9.

Kubilay, A., Bourcet, J., Gravel, J., Zhou, X., Moore, T.V., Lacasse, M.A., Carmeliet, J., Derome, D., 2021. Combined use of wind-driven rain load and potential evaporation to evaluate moisture damage risk: case study on the parliament buildings in Ottawa, Canada. Buildings 11 (10), 476.

Leckebusch, G.C., Renggli, D., Ulbrich, U., 2008. Development and application of an objective storm severity measure for the Northeast Atlantic region. Meteorol. Z. 575–587.

Little, A.S., Priestley, M.D., Catto, J.L., 2023. Future increased risk from extratropical windstorms in northern Europe. Nat. Commun. 14 (1), 4434.

Lowe, J.A., Bernie, D., Bett, P., Bricheno, L., Brown, S., Calvert, D., Clark, R., Eagle, K., Edwards, T., Fosser, G., Fung, F., 2018. UKCP18 Science Overview Report. Met Office Hadley Centre, Exeter, UK, pp. 1–73.

Ludwig, P., Pinto, J.G., Hoepp, S.A., Fink, A.H., Gray, S.L., 2015. Secondary cyclogenesis along an occluded front leading to damaging wind gusts: windstorm Kyrill, January 2007. Mon. Weather Rev. 143 (4), 1417–1437.

Manning, C., Widmann, M., Bevacqua, E., Van Loon, A.F., Maraun, D., Vrac, M., 2019. Increased probability of compound long-duration dry and hot events in Europe during summer (1950–2013). Environ. Res. Lett. 14 (9), 094006.

Manning, C., Kendon, E.J., Fowler, H.J., Roberts, N.M., Berthou, S., Suri, D., Roberts, M. J., 2022. Extreme windstorms and sting jets in convection-permitting climate simulations over Europe. Clim. Dynam. 58 (9–10), 2387–2404.

Manning, C., Kendon, E.J., Fowler, H.J., Roberts, N.M., 2023. Projected increase in windstorm severity and contribution from sting jets over the UK and Ireland. Weather Clim. Extrem. 40, 100562.

Martius, O., Pfahl, S., Chevalier, C., 2016. A global quantification of compound precipitation and wind extremes. Geophys. Res. Lett. 43 (14), 7709–7717.

Messmer, M., Simmonds, I., 2021. Global analysis of cyclone-induced compound precipitation and wind extreme events. Weather Clim. Extrem. 32, 100324.

Murphy, J.M., Harris, G.R., Sexton, D.M.H., Kendon, E.J., Bett, P.E., Clark, R.T., Yamazaki, K., 2018. UKCP18 land projections. Science report. Exeter, UK, *Met Office*.

Oertel, A., Sprenger, M., Joos, H., Boettcher, M., Konow, H., Hagen, M., Wernli, H., 2021. Observations and simulation of intense convection embedded in a warm conveyor belt–how ambient vertical wind shear determines the dynamical impact. Weather and Climate Dynamics 2 (1), 89–110.

O'Gorman, P.A., Schneider, T., 2009. The physical basis for increases in precipitation extremes in simulations of 21st-century climate change. Proc. Natl. Acad. Sci. USA 106 (35), 14773–14777.

Osinski, R., Lorenz, P., Kruschke, T., Voigt, M., Ulbrich, U., Leckebusch, G.C., Faust, E., Hofherr, T., Majewski, D., 2016. An approach to build an event set of European windstorms based on ECMWF EPS. Nat. Hazards Earth Syst. Sci. 16 (1), 255–268.

Owen, L.E., Catto, J.L., Dunstone, N.J., Stephenson, D.B., 2021a. How well can a seasonal forecast system represent three hourly compound wind and precipitation extremes over Europe? Environ. Res. Lett. 16 (7), 074019.

Owen, L.E., Catto, J.L., Stephenson, D.B., Dunstone, N.J., 2021b. Compound precipitation and wind extremes over Europe and their relationship to extratropical cyclones. Weather Clim. Extrem. 33, 100342.

Pfahl, S., Wernli, H., 2012. Quantifying the relevance of cyclones for precipitation extremes. J. Clim. 25 (19), 6770–6780.

Pfahl, S., 2014. Characterising the relationship between weather extremes in Europe and synoptic circulation features. Nat. Hazards Earth Syst. Sci. 14 (6), 1461–1475.

Pfahl, S., Madonna, E., Boettcher, M., Joos, H., Wernli, H., 2014. Warm conveyor belts in the ERA-Interim dataset (1979–2010). Part II: moisture origin and relevance for precipitation. J. Clim. 27 (1), 27–40.

Prein, A.F., Langhans, W., Fosser, G., Ferrone, A., Ban, N., Goergen, K., Keller, M., Tölle, M., Gutjahr, O., Feser, F., Brisson, E., 2015. A review on regional convection-permitting climate modeling: Demonstrations, prospects, and challenges. Rev. Geophys. 53 (2), 323–361.

Priestley, M.D., Catto, J.L., 2022a. Future changes in the extratropical storm tracks and cyclone intensity, wind speed, and structure. Weather and Climate Dynamics 3 (1), 337–360.

Priestley, M.D., Catto, J.L., 2022b. Improved representation of extratropical cyclone structure in HighResMIP models. Geophys. Res. Lett. 49 (5), e2021GL096708.

Raveh-Rubin, S., Wernli, H., 2015. Large-scale wind and precipitation extremes in the Mediterranean: a climatological analysis for 1979–2012. Q. J. R. Meteorol. Soc. 141 (691), 2404–2417.

Raveh-Rubin, S., Wernli, H., 2016. Large-scale wind and precipitation extremes in the Mediterranean: dynamical aspects of five selected cyclone events. Q. J. R. Meteorol. Soc. 142 (701), 3097–3114.

Raveh-Rubin, S., Catto, J.L., 2019. Climatology and dynamics of the link between dry intrusions and cold fronts during winter, Part II: front-centred perspective. Clim. Dynam. 53 (3–4), 1893–1909.

Ridder, N.N., Pitman, A.J., Westra, S., Ukkola, A., Do, H.X., Bador, M., Hirsch, A.L., Evans, J.P., Di Luca, A., Zscheischler, J., 2020. Global hotspots for the occurrence of compound events. Nat. Commun. 11 (1), 5956.

Ridder, N.N., Ukkola, A.M., Pitman, A.J., Perkins-Kirkpatrick, S.E., 2022. Increased occurrence of high impact compound events under climate change. Npj Climate and Atmospheric Science 5 (1), 3.

Sansom, P.G., Catto, J.L., 2022. Improved objective identification of meteorological fronts: a case study with ERA-Interim. Geosci. Model Dev. Discuss. (GMDD) 1–19.

Schemm, S., Wernli, H., 2014. The linkage between the warm and the cold conveyor belts in an idealized extratropical cyclone. J. Atmos. Sci. 71 (4), 1443–1459.

Schultz, D.M., 2001. Reexamining the cold conveyor belt. Mon. Weather Rev. 129 (9), 2205–2225.

Screen, J.A., Eade, R., Smith, D.M., Thomson, S., Yu, H., 2022. Net equatorward shift of the jet streams when the contribution from sea-ice loss is constrained by observed eddy feedback. Geophys. Res. Lett. 49 (23), e2022GL100523.

Shepherd, T.G., 2014. Atmospheric circulation as a source of uncertainty in climate change projections. Nat. Geosci. 7 (10), 703–708.

Sinclair, V.A., Rantanen, M., Haapanala, P., Räisänen, J., Järvinen, H., 2020. The characteristics and structure of extra-tropical cyclones in a warmer climate. Weather and Climate Dynamics 1 (1), 1–25.

Sklar, M., 1959. Fonctions de répartition à n dimensions et leurs marges. Annales de l'ISUP 8 (3), 229–231.

Støver, E.A., Sundsøy, M.H., Andenæs, E., Geving, S., Kvande, T., 2022. Rain intrusion through horizontal joints in Façade panel systems—Experimental Investigation. Buildings 12 (10), 1497.

Tamarin-Brodsky, T., Kaspi, Y., 2017. Enhanced poleward propagation of storms under climate change. Nat. Geosci. 10 (12), 908–913.

Tilloy, A., Malamud, B.D., Joly-Laugel, A., 2022. A methodology for the spatiotemporal identification of compound hazards: wind and precipitation extremes in Great Britain (1979–2019). Earth System Dynamics 13 (3), 993–1020.

Utsumi, N., Kim, H., Kanae, S., Oki, T., 2017. Relative contributions of weather systems to mean and extreme global precipitation. J. Geophys. Res. Atmos. 122 (1), 152–167.

Vignotto, E., Engelke, S., Zscheischler, J., 2021. Clustering bivariate dependencies of compound precipitation and wind extremes over Great Britain and Ireland. Weather Clim. Extrem. 32, 100318.

Ward, P.J., Couasnon, A., Eilander, D., Haigh, I.D., Hendry, A., Muis, S., Veldkamp, T.I., Winsemius, H.C., Wahl, T., 2018. Dependence between high sea-level and high river discharge increases flood hazard in global deltas and estuaries. Environ. Res. Lett. 13 (8), 084012.

Woollings, T., Drouard, M., O'Reilly, C.H., Sexton, D.M., McSweeney, C., 2023. Trends in the atmospheric jet streams are emerging in observations and could be linked to tropical warming. Communications Earth & Environment 4 (1), 125.

Zappa, G., Shaffrey, L.C., Hodges, K.I., Sansom, P.G., Stephenson, D.B., 2013. A multimodel assessment of future projections of North Atlantic and European extratropical cyclones in the CMIP5 climate models. J. Clim. 26 (16), 5846–5862.

Zappa, G., 2019. Regional climate impacts of future changes in the mid–latitude atmospheric circulation: a storyline view. Curr. Clim. Change Rep. 5, 358–371.

Zhou, X., Derome, D., Carmeliet, J., 2016. Robust moisture reference year methodology for hygrothermal simulations. Build. Environ. 110, 23–35.

Zscheischler, J., Westra, S., Van Den Hurk, B.J., Seneviratne, S.I., Ward, P.J., Pitman, A., AghaKouchak, A., Bresch, D.N., Leonard, M., Wahl, T., Zhang, X., 2018. Future climate risk from compound events. Nat. Clim. Change 8 (6), 469–477.

Zscheischler, J., Naveau, P., Martius, O., Engelke, S., Raible, C.C., 2021. Evaluating the dependence structure of compound precipitation and wind speed extremes. Earth system dynamics 12 (1), 1–16.